



An IFU View of the Active Galactic Nuclei in MaNGA Galaxy Pairs

Gaoxiang Jin^{1,2}, Y. Sophia Dai¹, Hsi-An Pan³, Lihwai Lin⁴, Cheng Li⁵, Bau-Ching Hsieh⁴, Shiyin Shen⁶, Fang-Ting Yuan⁶, Shuai Feng^{6,7,8}, Cheng Cheng¹, Hai Xu¹, Jia-Sheng Huang¹, and Kai Zhang⁹

¹ Chinese Academy of Sciences South America Center for Astronomy (CASSACA), National Astronomical Observatories(NAO), 20A Datun Road, Beijing 100012, People's Republic of China; ydai@nao.cas.cn

² University of Chinese Academy of Sciences (UCAS), Beijing, 100049, People's Republic of China

³ Max-Planck-Institut für Astronomie, Königstuhl 17, D-69117 Heidelberg, Germany

⁴ Institute of Astronomy and Astrophysics, Academia Sinica, Taipei 10617, Taiwan

⁵ Department of Astronomy, Tsinghua University, Beijing 100084, People's Republic of China

⁶ Key Laboratory for Research in Galaxies and Cosmology, Shanghai Astronomical Observatory, Chinese Academy of Sciences, 80 Nandan Road, Shanghai 200030, People's Republic of China

⁷ College of Physics, Hebei Normal University, 20 South Erhuan Road, Shijiazhuang 050024, People's Republic of China

⁸ Hebei Key Laboratory of Photophysics Research and Application, Shijiazhuang 050024, People's Republic of China

⁹ Lawrence Berkeley National Laboratory, 1 Cyclotron Road, Berkeley, CA 94720, USA

Received 2021 May 30; revised 2021 September 14; accepted 2021 September 20; published 2021 December 7

Abstract

The role of active galactic nuclei (AGNs) during galaxy interactions and how they influence the star formation in the system are still under debate. We use a sample of 1156 galaxies in galaxy pairs or mergers (hereafter “pairs”) from the MaNGA survey. This pair sample is selected by the velocity offset, projected separation, and morphology, and is further classified into four cases along the merger sequence based on morphological signatures. We then identify a total of 61 (5.5%) AGNs in pairs based on the emission-line diagnostics. No evolution of the AGN fraction is found, either along the merger sequence or compared to isolated galaxies (5.0%). We observe a higher fraction of passive galaxies in galaxy pairs, especially in the pre-merging cases, and associate the higher fraction to their environmental dependence. The isolated AGN and AGNs in pairs show similar distributions in their global stellar mass, star-formation rate (SFR), and central [O III] surface brightness. AGNs in pairs show radial profiles of increasing specific SFR and declining Dn4000 from center to outskirts, and no significant difference from the isolated AGNs. This is clearly different from star-forming galaxies (SFGs) in our pair sample, which show enhanced central star formation, as reported before. AGNs in pairs have lower Balmer decrements at outer regions, possibly indicating less dust attenuation. Our findings suggest that AGNs are likely follow an inside-out quenching and the merger impact on the star formation in AGNs is less prominent than in SFGs.

Unified Astronomy Thesaurus concepts: Active galactic nuclei (16); AGN host galaxies (2017); Galaxy mergers (608); Galaxy interactions (600); Star formation (1569); Galaxy evolution (594)

1. Introduction

Galaxy–galaxy interaction plays an important role in the evolution of galaxies. Theoretically, the merging of galaxies will result in the in-fall of gas toward the center and trigger central star formation (Barnes & Hernquist 1991; Blumenthal & Barnes 2018). Several numerical simulations (e.g., Kauffmann & Haehnelt 2000; Di Matteo et al. 2005; Hopkins et al. 2006a, 2006b; Gabor et al. 2016; Capelo et al. 2017) also predicted the emergence of active galactic nuclei (AGNs) in galaxy mergers. According to simulations, the merging of two gas-rich ($M_{\text{gas}} = 20\% M_*$, e.g., Hopkins et al. 2006a) equal-mass galaxies will drive the gas into the center owing to the loss of angular momentum. The supply of infalling gas to the center will fuel both nuclear starbursts and the growth of supermassive black holes (SMBHs), which would experience several peaks from the first encounter to the final coalescence (e.g., Hopkins et al. 2006b).

To study the merger effects from an observational view, ideally we should build an ongoing merger sample along the merger sequence. There are several approaches to build a merger sample, but all have pros and cons. For example, by selecting galaxy pairs through projected separation and velocity offset (e.g., Patton et al. 2002; Lin et al. 2004), one can build statistically significant galaxy pair samples from large spectroscopic surveys (e.g., Ellison et al. 2008; Alpaslan et al. 2015;

Shen et al. 2016; Feng et al. 2019). But this method requires spectroscopic redshifts and these samples often suffer from incompleteness issues (e.g., Patton & Atfield 2008). Visual classification (e.g., Willett et al. 2013; Kartaltepe et al. 2015) is a powerful tool to select the late-stage and post merging systems which could be missed in spectroscopic pairs. Machine learning is a recent, effective method (e.g., Ackermann et al. 2018; Domínguez Sánchez et al. 2018; Pearson et al. 2019; Walmsley et al. 2019). However, due to the limitation of training sets (e.g., Bottrell et al. 2019), the machine-learning method is yet to achieve a high accuracy compared to visual classifications. Most current works, including this one, still adopt the physical selection of pairs followed by visual classification. Combining these two methods includes both galaxy pairs and late-stage mergers. Hereafter, for convenience, we refer to both galaxy pairs and merger systems as galaxy “pairs.”

In galaxy pairs, the enhancement of star formation has been widely observed, often based on the comparison of the star-formation rate (SFR) with isolated control galaxies. These enhancements have been found in various SFR indicators, including stronger emission lines (e.g., Kennicutt et al. 1987; Barton et al. 2000; Lambas et al. 2003; Woods et al. 2006, 2010; Li et al. 2008a), bluer colors (e.g., Larson & Tinsley 1978; Patton et al. 2005, 2011; Lin et al. 2007; Smith & Struck 2010),

and stronger infrared emission (e.g., Xu & Sulentic 1991; Sanders & Mirabel 1996; Geller et al. 2006; Hwang et al. 2011). The level of enhancements varies with pairs' mass ratios (Ellison et al. 2008) or with different morphologies (e.g., Xu et al. 2010; Yuan et al. 2012).

According to simulations and theoretical predictions, mergers are expected to facilitate the accretion onto the central SMBHs, and trigger AGNs (e.g., Hopkins et al. 2006a). Observationally, enhanced AGN luminosity is found in galaxy pairs. Compared to isolated galaxies, [O III] luminosity, a proxy for AGN luminosity, is found to increase by 0.7–0.9 dex in pairs (e.g., Liu et al. 2012; Ellison et al. 2013; Alonso et al. 2018). Similarly, AGNs in galaxy pairs are found to have a higher X-ray detection rate (58%) than AGN in isolated galaxies (17%, Hou et al. 2020). In addition, mergers appear to play a dominant role in the triggering and fueling of high-luminosity AGNs. The most luminous AGNs are often found to be associated with signatures of merging, such as tidal tails, asymmetric morphology, bridges, and shells. Using deep and high-resolution Hubble Space Telescope imaging, interaction features have been found in various quasar samples: in more than 80% of AGNs selected from the FIRST-2MASS red quasar survey (Urrutia et al. 2008; Glikman et al. 2015), in four out of the five nearby early-type quasars from Bennert et al. (2008), in 57% of the Palomar-Green quasars (Veilleux et al. 2009), and in 62% of the hosts of highly obscured AGNs (Fan et al. 2016). Donley et al. (2018) found that in the CANDLES/COSMOS field, compared with X-ray AGNs, infrared selected AGNs are more likely to have disturbed morphologies.

Another evidence for merger-triggered AGN activities is the increased AGN fractions in galaxy pairs. However, this evidence is still inconclusive as different results have been found. For instance, in optically selected AGNs in galaxy pairs, the AGN fraction enhancement has been reported in several studies to be $1.4 \times$ – $2.4 \times$ in some studies (e.g., Keel et al. 1985; Woods & Geller 2007; Ellison et al. 2011, 2013), but not in other samples (e.g., Schmitt 2001; Coldwell & Lambas 2006; Alonso et al. 2007; Ellison et al. 2008; Darg et al. 2010). For X-ray-selected AGNs, AGN fraction enhancement has been reported found in Silverman et al. (2011), Lackner et al. (2014), and Secrest et al. (2020), but not in a much larger sample of Shah et al. (2020). As for AGNs that are infrared color selected, most works have found a higher AGN fraction in pairs than in an isolated control sample (e.g., Satyapal et al. 2014; Weston et al. 2017; Goulding et al. 2018; Ellison et al. 2019; Gao et al. 2020). In addition, Argudo-Fernández et al. (2016) found more radio AGNs in pair or cluster environments. Recently, Silva et al. (2021) built a multiwavelength sample including optical, X-ray, infrared, and radio-selected AGNs, but found no AGN fraction excess in galaxy pairs. Various factors, such as different pair selections, control sample selections, the sizes of the sample, the redshift bins, and the different merger stages could all contribute to the diverse observation results.

Most previous work focused on galaxies' global properties, due to the lack of spatially resolved spectra. Integral field unit (IFU) observations offer a new opportunity to study thousands of nearby galaxies in sub-galactic scales (e.g., Sánchez 2020). For instance, the MaNGA (mapping nearby galaxies at Apache Point Observatory, Bundy et al. 2015) survey is one of the largest IFU survey, which has observed $\sim 10,000$ galaxies at redshift of ~ 0.02 – 0.1 . IFU surveys have two advantages to study galaxy pairs: (1) their high spatial sampling spectra allow

the confirmation of the accurate velocity offset between galaxies, and we can identify the pairs with very small projected separations; (2) IFU observations also offer two-dimensional dynamical information, so that we can analyze the resolved properties of the pair systems. Several works have taken advantage of IFU to study the spatial extent of star formation in star-forming galaxy (SFG) pairs or mergers (e.g., Knapen & James 2009; Schmidt et al. 2013; Wild et al. 2014; Barrera-Ballesteros et al. 2015a; Yuan et al. 2018; Pan et al. 2019; Thorp et al. 2019; Steffen et al. 2021), and have found enhanced SFR at different radii of interacting SFGs. Specifically, Thorp et al. (2019) found a centrally peaked SFR enhancement and general metallicity suppression in MaNGA star-forming post-mergers; while Pan et al. (2019) found that the SFR enhancement in SFGs pairs emerges after the first encounter. In addition, morphologically, Li et al. (2021) found a higher pair fraction in both SFGs and quiescent galaxies that show misaligned gas-stellar rotation. Feng et al. (2020) showed that galaxies in pairs have higher kinematic asymmetry.

IFU studies on the AGN properties in galaxy pairs, on the other hand, are still lacking. Using earlier MaNGA data, Fu et al. (2018) found 14 AGN binaries and discovered an increase of binary AGN systems in pairs with smaller separations, but no analysis on the resolved properties was performed. Bing et al. (2019) showed that MaNGA AGNs have centrally suppressed star formation. Whether star formation (SF) is enhanced or suppressed in pairs with AGN remains an open question.

With the MaNGA survey, we now construct the largest IFU sample of galaxy pairs with AGNs. In this paper, we aim to study the sub-galactic properties including star formation, age, and extinction in galaxy pairs with one or both AGNs, to understand the merger effects on the star-formation condition of these AGN host galaxies. In addition, we will also classify our sample into different merger cases in order to study the change of AGN fraction and galaxies' resolved SF properties along the merger sequence. This paper is structured as follows. Section 2 is the data overview, discussing pair sample selection, merger-sequence definition, and control sample selection. In Section 3, we select the AGNs in our sample and study their fractions along the merger sequence. In Section 4, we present the global and resolved properties of our sample, and compare them with isolated control samples. We compare our work with previous work and discuss the selection biases and caveats in Section 5. We summarize our results in Section 6. Throughout this paper, we use the AB magnitude system (Oke & Gunn 1983), the Salpeter initial mass function (IMF, Salpeter 1955), and adopt a Λ CDM cosmology with $\Omega = 0.3$, $\Lambda = 0.7$, and $H_0 = 70 \text{ km s}^{-1} \text{ Mpc}^{-1}$.

2. Sample Overview

2.1. The MaNGA Data

MaNGA is one of the major surveys of SDSS-IV (The fourth-generation Sloan Digital Sky Survey; Blanton et al. 2017), which aims to obtain resolved spectroscopy for $\sim 10,000$ nearby galaxies (Law et al. 2015), using 17 science IFUs (Drory et al. 2015) over the 2.5 m Sloan Telescope's 3° diameter field of view (FOV). These IFUs vary in diameter from $12''$ to $32''$ (19 to 127 fibers). Each $2''$ fiber has a spatial resolution of ~ 1 kpc at the peak redshift of $z \sim 0.03$. MaNGA's observed wavelength range (3600–10300 Å) can cover most

strong nebular lines out to $z \sim 0.4$. This includes the important lines used in the BPT excitation diagnostic diagram (Baldwin et al. 1981), which is widely used to identify galaxy types between AGNs and SFGs. MaNGA has spectral resolution that varies from $R \sim 1400$ at 4000 Å to $R \sim 2600$ at 9000 Å (Yan et al. 2016a). Target galaxies are covered out to at least 1.5 effective radius (R_e , Yan et al. 2016b). MaNGA’s parent sample is made of 641,409 galaxies with spectroscopic data from NASA-Sloan-Atlas¹⁰, based on the SDSS DR7 main galaxy sample (Abazajian et al. 2009). Detailed target selection for MaNGA can be found in Wake et al. (2017).

Our sample is drawn from the public data release MaNGA Product Launch-6 (MPL-6 and SDSS DR15), which contains 4691 IFU observations within the survey’s first four years of operation. The emission-lines and spectral indices are from data analysis pipeline (DAP, Belfiore et al. 2019; Westfall et al. 2019), the official high level data product of MaNGA. DAP uses the stellar templates from MILES library (medium-resolution Isaac Newton telescope library of empirical spectra, Sánchez-Blázquez et al. 2006; Falcón-Barroso et al. 2011) and adopts the pPXF (penalized pixel-fitting, Cappellari & Emsellem 2004; Cappellari 2017) as the spectral-fitting routine. The integrated and resolved dust-corrected stellar masses are taken from Pipe3D¹¹ (Sánchez et al. 2016a, 2016b, 2018), another model-derived MaNGA data product.

2.2. Identification of Galaxy Pair Systems

MaNGA galaxies and most of their neighbors have spectroscopic redshifts from SDSS single-fiber spectra. We adopt a two-step pair selection, first based on projected distances and velocity offsets, and then the late-stage mergers are visually selected. These two steps allow us to select galaxy pairs from the incoming merging phase until the final coalescence. Similar to other pair selections (e.g., Patton et al. 2002; Lin et al. 2004; Pan et al. 2019), galaxies in our pair sample are required to have a close spectroscopic companion at a projected separation $\Delta d < 50 \text{ kpc h}^{-1}$ (i.e., 71.4 kpc) and a line-of-sight velocity difference $\Delta v < 500 \text{ km s}^{-1}$. This method misses mergers at their late merging stage due to the lack of the redshifts of the companions, or mergers in the coalescence stage, where only one source is identified. Therefore, we also visually check all MPL-6 galaxies and identify the missing late-stage pairs or mergers based on their morphology from the SDSS *gri* images. Out of the 4622 (of 4691) unique MaNGA MPL-6 targets, we eventually identify 994 unique galaxy pair systems, with a total of 1156 galaxies covered in MaNGA. This is the same parent sample as in Pan et al. (2019). Among these 994 galaxy pairs/mergers, 46 pairs have individual IFU coverage for both member galaxies; 116 pairs have both members covered in the same IFU cube; 125 are mergers in late-stage coalescence covered with one single IFU cube; and the remaining 707 pair systems have only one member galaxy with a MaNGA IFU coverage.

2.3. Merger-sequence Definition

Simulations have predicted that the merging of two galaxies would experience several passages before the final coalescence (e.g., Toomre & Toomre 1972; Barnes 1988; Barnes & Hernquist 1992).

Thus, the projected separation alone is not sufficient to define the merger sequence. Therefore, we combine the kinematic information with the morphological features to classify the merger stages and divide our sample into four cases, to represent the possible merger sequences, the same as Pan et al. (2019). The classification follows the following criteria:

1. Case 1—Well-separated pairs that do not show any morphology distortion (i.e., incoming pairs, before the first pericenter passage).
2. Case 2—Close pairs showing strong signs of interaction, such as tidal tails and bridges (i.e., likely at the first pericenter passage).
3. Case 3—Well-separated pairs, showing weak morphology distortion (i.e., approaching the apocenter or just passing the apocenter).
4. Case 4—Two components strongly overlapping with each other and showing strong morphological distortion (i.e., final coalescence phase), or single galaxies with obvious tidal features such as tails and shells (post-mergers).

Each pair candidate is visually classified by four expert classifiers and placed into the above four cases. The classification result is decided by the majority if possible, otherwise it is discussed on an individual basis by all inspectors (this only applies to $\sim 5\%$ of objects in our sample). We note that although Case 1 and Case 4 represent the incipient and final stages of the merging galaxies, the relative chronological order of Case 2 and Case 3 is not clear. Therefore, in order to avoid confusion, we refer to them as “case” instead of “stages.” We reach a final parent sample of 441 unique pair systems in Case 1, 119 in Case 2, 265 in Case 3, and 169 in Case 4. Figure 1 shows illustrations of examples of SDSS *gri*-composite images, for each case and for isolated galaxies. The galaxy morphology in each case is consistent with the morphological signatures of the Toomre Sequence (Toomre 1977, also see Veilleux et al. 2002 and Barrera-Ballesteros et al. 2015b), and in simulated mergers (e.g., Figure 8 in Torrey et al. 2012 and Figure 2 in Moreno et al. 2015). Factors other than morphology may affect the SF properties in pairs, such as the encounter geometry (e.g., Di Matteo et al. 2007), mass ratio (e.g., Cox et al. 2008), gas richness (e.g., Scudder et al. 2015; Violino et al. 2018), and the relative morphological types of the member galaxies (e.g., Cao et al. 2016). We do not control these factors in our merger-sequence classification due to our limited sample size.

2.4. Control Samples

To better estimate the effect of merging for various physical parameters, control samples of isolated galaxies are needed. In order to define the various control samples, we first select galaxies without a physical companion ($\Delta d > 150 \text{ kpc h}^{-1}$ or $\Delta v > 500 \text{ km s}^{-1}$) in MaNGA. This way we construct a parent sample of 2317 isolated galaxies. The SFR is known to increase with the stellar mass, as shown in the star-formation main sequence (SFMS, e.g., Noeske et al. 2007). To make a fair comparison of the SF conditions in the various samples with limited mass effect, we further define the control samples on a mass-controlled basis. Based on the galaxy types and similar stellar mass requirement, we build a series of control samples from the parent isolated sample, namely, the isolated AGN sample, the isolated SFG sample, and the isolated passive

¹⁰ NSA; M. Blanton; <http://www.nsatlas.org/>.

¹¹ https://data.sdss.org/datamodel/files/MANGA_PIPE3D/MANGADRP_VER/PIPE3D_VER

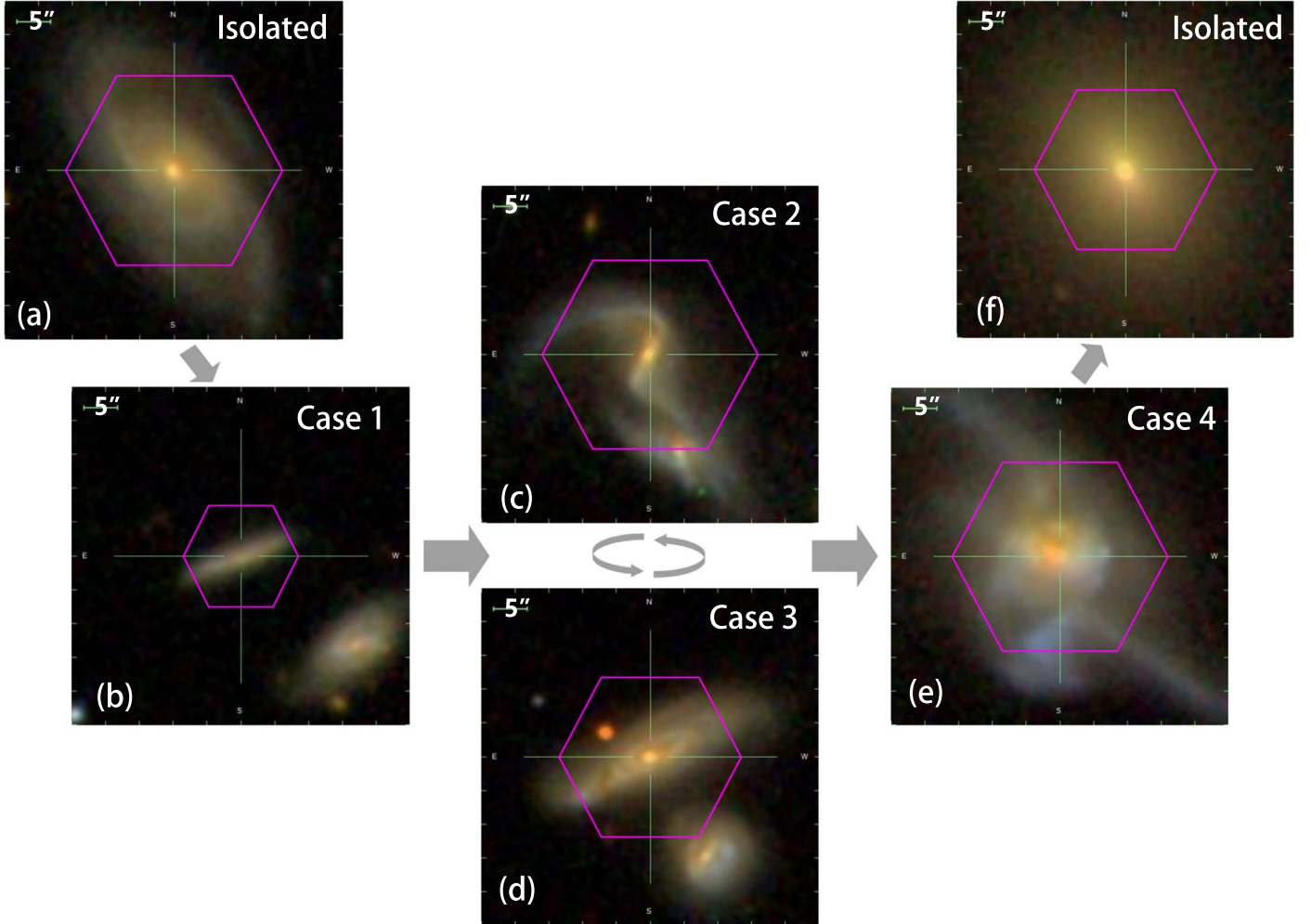


Figure 1. Illustration of the possible merger sequence. Examples of the SDSS *gri*-composite color images for the four merging cases (b), (c), (d), (e) and isolated galaxies (a), (f). The MaNGA Plate-IFU numbers are (a): 9500–12702; (b): 8485–3704; (c): 8241–12705; (d): 8082–9102; (e): 9507–12704; (f): 8984–9101, respectively. The magenta hexagons mark the corresponding IFU’s FOV. The arrows indicate the possible merger sequence among our four merger cases and between isolated galaxies.

Table 1
Information of the Various Subsamples and their Relevant Control Samples

Related Figure(s)	Subsample	Number of Galaxies (total)	Mass Range $\log(M_*/M_\odot)$	Median Mass $\log(M_*/M_\odot)$	K-S test p
Paired AGN versus Isolated AGN (Figures 4, 5, 6, 7)	AGNs in pairs	61	9.94–11.55	10.93	/
	Isolated AGNs	116	9.93–11.70	10.80	0.05
AGN versus SFG (Figure 8)	AGNs in pairs	34	10.11–10.97	10.73	/
	Isolated AGNs	36	10.11–10.97	10.73	0.99
	SFGs in pairs	50	10.11–10.97	10.68	0.38
	Isolated SFGs	101	10.12–10.97	10.66	0.40
AGN versus passive galaxy (Figure 9)	AGNs in pairs	61	9.94–11.55	10.93	/
	Isolated AGNs	71	10.11–11.40	10.84	0.33
	Passive in pairs	311	9.95–11.55	11.00	0.50
	Isolated Passive	352	9.94–11.55	10.94	1.00

Note. Information of the control samples used in different analysis. From left to right: the names of the subsamples, total numbers of galaxies, mass ranges, median stellar masses, and K-S test p values as compared to the paired AGN subsample (bold font).

galaxy sample (for various galaxies’ definition, see Section 3.1). Table 1 summarizes the various subsamples used in the following analysis, as well as the Kolmogorov–Smirnov (K-S) test probability p values of the relative stellar mass

distributions to the pair subsamples. Given the intrinsic different mass distributions between the AGN and SFGs, to make a fair comparison of their radial profiles in Section 4.3, we further require that both the AGN and SFG subsamples to

have a stellar mass between $10^{10.0} - 10^{11.0} M_{\odot}$. Similarly, for the comparison between AGN and the passive galaxies (retired galaxies and lineless galaxies), we also require the similar mass distribution and limit their stellar mass to be between $10^{9.9} - 10^{11.6} M_{\odot}$.

3. AGN Classification

3.1. Emission-line Classification

Nebular emission-lines from the narrow line region (NLR) of an AGN show different flux ratios from those from H II regions, and are widely used to classify AGNs from SFGs. With MaNGA's high quality spectra, we adopt various emission-line diagnostics to classify the AGNs. In this work, we use both the original [N II]-BPT (Baldwin et al. 1981) and the modified [S II]-BPT diagrams (Veilleux & Osterbrock 1987), which utilize combinations of the $[\text{O III}]_{\lambda 5007}/\text{H}\beta$ versus $[\text{N II}]_{\lambda 6584}/\text{H}\alpha$ and $[\text{O III}]_{\lambda 5007}/\text{H}\beta$ versus $[\text{S II}]_{\lambda \lambda 6716, 6731}/\text{H}\alpha$ line ratios. We also adopt the $\text{H}\alpha$ equivalent width (EW) versus $[\text{N II}]_{\lambda 6584}/\text{H}\alpha$ diagram (WHAN, Cid Fernandes et al. 2010) to single out “retired galaxies” (RGs).

Given the fact that SMBHs locate in the center of galaxies, we use the mean value of the central 3×3 spaxels ($1.^{\prime\prime}5 \times 1.^{\prime\prime}5$) of the galaxy, for emission-line-based classifications. Therefore, the galaxy types reported here represent the galaxies' nuclear properties. “AGN-like” spaxels in the outskirts of a galaxy will not be considered. For instance, if a galaxy does not have emission-line features in the central region, but has strong star-forming regions in the disk or outskirt, it will still be classified as a lineless galaxy.

In the [N II]-BPT diagram (Figure 2, (a)), the dashed curve (Equation(1), Ke01a) marks the starburst line from Kewley et al. (2001) and the solid curve marks the empirical separation between AGNs and SFGs from Equation(2) from Kauffmann et al. (2003). Star-forming galaxies locate below the Ke01a curve and AGN-like galaxies locate above the Ka03 curve. Galaxies between these two curves are considered to have radiation contribution from both the star formation and the SMBH accretion (Kauffmann & Heckman 2009), and are considered as “composite” galaxies. We find that most of the composite galaxies are indeed in the star-forming region of the [S II]-BPT diagram. To avoid the contamination from SFGs, we restrict our AGN selections to only the AGN regions (see Figure 2), and do not include the composite galaxies in the [N II]-BPT diagram. The separation curves for the [N II]- and [S II]-BPT diagrams are summarized below:

$$\log([\text{O III}]/\text{H}\beta) = \frac{0.61}{\log([\text{N II}]/\text{H}\alpha) - 0.47} + 1.19; \text{ Ke01a} \quad (1)$$

$$\log([\text{O III}]/\text{H}\beta) = \frac{0.61}{\log([\text{N II}]/\text{H}\alpha) - 0.05} + 1.30; \text{ Ka03} \quad (2)$$

$$\log([\text{O III}]/\text{H}\beta) = \frac{0.72}{\log([\text{S II}]/\text{H}\alpha) - 0.32} + 1.30; \text{ Ke01b} \quad (3)$$

Since the hot evolved stellar populations such as post-AGB stars can also produce similar line ratios in the AGN region of the BPT diagrams (Binette et al. 1994; Yan & Blanton 2012), we further remove the “inactive” galaxies from our AGN

sample based on the WHAN diagram. The WHAN diagram is based on the fact that the EW of $\text{H}\alpha$ ($\text{H}\alpha$ EW) is a robust proxy for measuring the photoionization by stellar populations older than 100 Myr (Cid Fernandes et al. 2011). We adopt the suggested empirical division between RGs and AGNs at 3 \AA , and only keep galaxies with $\text{H}\alpha$ EW $\geq 3 \text{ \AA}$ in our final AGN sample.

To summarize, our AGN selections in the nuclear region follow these criteria:

1. We require all emission-lines used in the BPT diagram ($\text{H}\alpha$, $\text{H}\beta$, $[\text{O III}]$, $[\text{N II}]$, or $[\text{S II}]$) to have a signal-noise-ratio (S/N) greater than 5. If a galaxy's central region has a well fitted continuum but the S/N of $\text{H}\alpha$ is lower than 5, or includes weak or no $\text{H}\alpha$ emission, it will be classified as a lineless galaxy.
2. We use the WHAN diagram to select RGs, defined as galaxies with nuclear $\text{H}\alpha$ EW $< 3 \text{ \AA}$, regardless of their positions in the BPT diagrams.
3. For galaxies with $\text{H}\alpha$ EW $\geq 3 \text{ \AA}$, we classify the galaxy as an AGN if it falls in either the [N II]-AGN or the [S II]-AGN regions. In our final sample of 61 AGNs in pairs, a total of 43 galaxies are classified as AGNs by both BPT criteria, while 6 are AGNs only selected in the [N II]-BPT diagram, and 12 are selected in the [S II]-BPT diagram only.
4. We then use the [N II]-BPT diagram to classify composite galaxies and SFGs.

The classification results for all MaNGA galaxies are listed in Table 3. The results of the three diagnostic diagrams (BPT, modified BPT, and WHAN, Figures 2 (a), (b), and (c)) are generally consistent (88%) with each other. For comparison, we also plot the positions of our galaxies in the color-magnitude diagram (Figure 2(d)). In Figure 2(d), we also draw the division lines from Wyder et al. (2007) to guide the eyes of the three regions defined as: “red sequence,” “green valley (GV),” and “blue cloud.” We find that, in Figure 2(d), SFGs (blue) and RGs (black) lie mostly in the “blue cloud” and “red sequence,” respectively; while AGNs (red) and composite galaxies (green) tend to lie in the “green valley,” indicating that the AGNs in our sample are in possible transition from the blue cloud to the red sequence. We note that our AGN sample, like other BPT-selected AGN samples, is biased against AGNs with broad emission lines, or in very dusty systems with significant extinction of the emissions from the NLR, as well as radio AGNs without emission-lines (see Padovani et al. 2017, for a review).

3.2. AGN Fractions along the Merger Sequence

In this section, we compare the AGN fractions along the merger sequence (for definition, see Section 2.3) from Case 1 to Case 4, as well as in the isolated galaxies. MPL-6 includes 4620 unique IFU cubes, out of which there are 116 IFU cubes that cover two galaxies in a pair (see Section 2.2). Therefore, in the full MPL-6 parent sample, we classify 4736 galaxies. A total of 187 galaxies' DAP products are marked as not suitable for scientific use due to the contamination of foreground stars, uncertainties in redshift, or other critical failures. After removing these galaxies, we classify the remaining 4549 galaxies (including 1115 galaxies in pairs) following the same criteria listed in Section 3, and find 239 (5.3%) AGNs, 385 (8.5%) AGN-starburst composites, 1654 (36.4%) SFGs, 1267

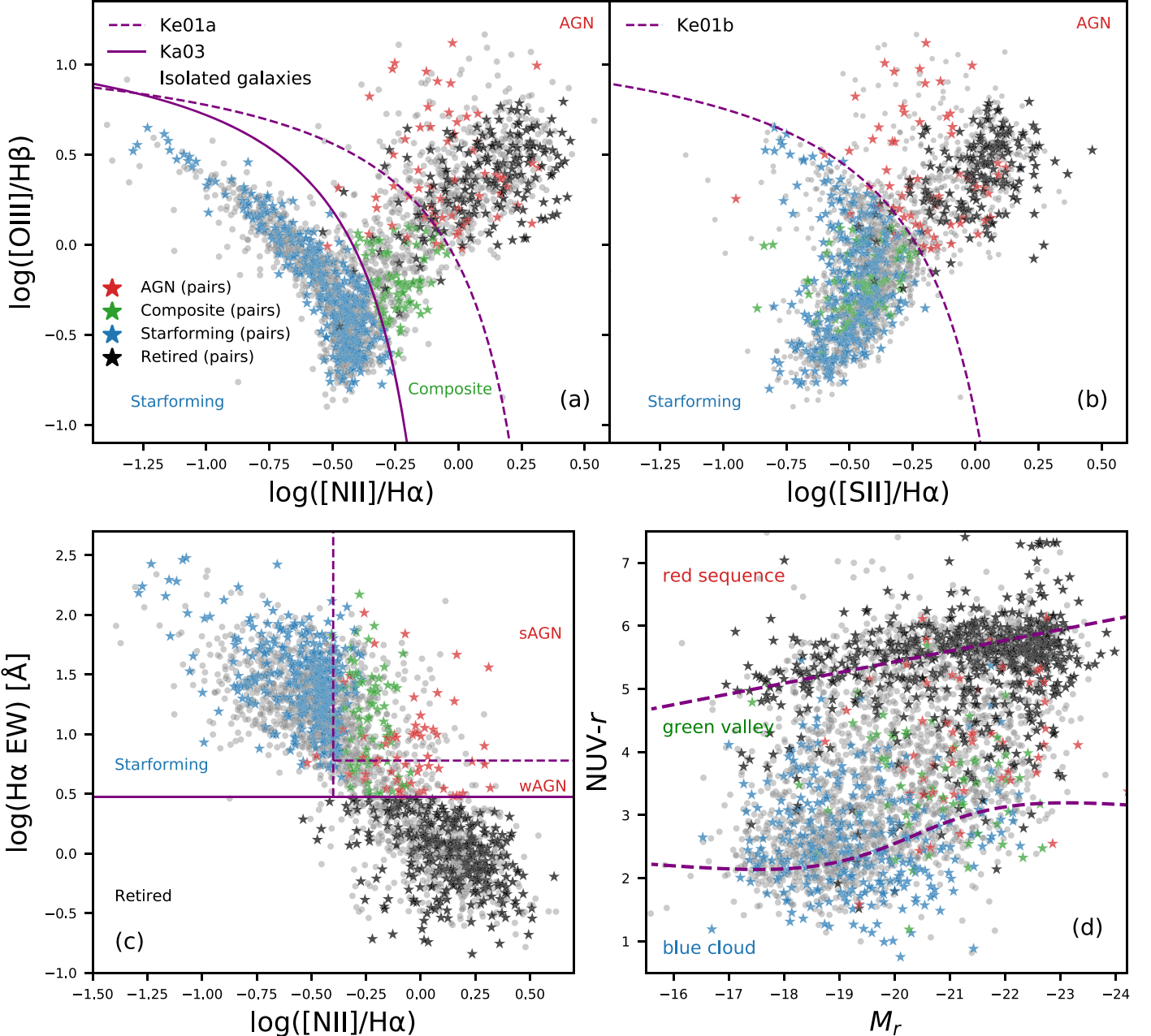


Figure 2. The (a) original and (b) modified BPT diagrams. (c) The WHAN diagram and (d) NUV- r vs. M_r color-magnitude diagram using k-corrected magnitudes from the NSA catalog. The gray dots are all the BPT-classified isolated MaNGA MPL-6 galaxies. Galaxies in pairs are plotted as colored stars, with red for AGNs, green for composite galaxies, blue for SFGs, and black for retired galaxies. For (a) and (b), the dividing curves are from Kewley et al. (2001) and Kauffmann et al. (2003) and relevant galaxy types are marked in the corresponding panels. In (c), the dividing lines are from Cid Fernandes et al. (2011), which classifies the galaxies into SFGs, strong AGNs, weak AGNs, and retired galaxies. In (d), SFGs (blue), RGs (black), and AGNs (red) tend to lie in the “blue cloud,” “red sequence,” and “green valley” regions, respectively. The dividing lines are from Wyder et al. (2007), corrected for the underestimated NUV flux by 0.3 mag found in nearby galaxies (see footnote 12).

(27.8%) RGs, and 1004 (22.1%) lineless galaxies. In our pair sample (1115 galaxies), the corresponding numbers and fractions are 61 (5.5%), 74 (6.6%), 310 (27.8%), 313 (28.1%), 357 (32.0%). We list the physical parameters of the 61 AGNs in pairs in Table 2.

This $\sim 5.3\%$ AGN fraction found in the full MPL-6 is consistent with previous MaNGA works using the emission-line diagnostics (Rembold et al. 2017; Sánchez et al. 2018; Wylezalek et al. 2018), where an AGN fraction of $\sim 3\%-11\%$ was found in ~ 2700 galaxies from earlier MaNGA data release

of MPL-5. For MaNGA MPL-8, Comerford et al. (2020) built a sample of 406 AGNs (283 are from MPL-6), compiled through a combination of wide-field infrared survey explorer (WISE) mid-infrared color cuts, Swift/BAT hard X-ray detection, NVSS/FIRST 1.4 GHz radio sources, and SDSS broad emission-lines. Given the significantly different selection criteria, there are only 21% AGNs from Rembold et al. (2017), 13% AGNs from Wylezalek et al. (2018), 23% AGNs from Sánchez et al. (2018), and 22% from our AGN sample that overlap with the Comerford et al. (2020) sample. Among

Table 2
Parameters of the 61 AGNs in Galaxy Pairs

Plate-IFU (1)	R.A. ° (2)	Decl. ° (3)	z (4)	Merger Case (5)	$\log(M_*)$ $\log(M_\odot)$ (6)	$\log(\text{SFR})$ $\log(M_\odot \text{ yr}^{-1})$ (7)	Morphology (8)	$\Sigma_{[\text{O III}]}$ $\log(\text{erg s}^{-1} \text{ kpc}^{-2})$ (9)
7975-12702	323.5212	10.4219	0.0774	1	10.73	0.147	E	38.32
8132-6101	111.7337	41.0267	0.1294	3	11.55	0.980	SBb	39.92
8247-6101	136.0896	41.4817	0.0245	2	10.77	-0.551	E	37.83
8256-12704	166.1294	42.6246	0.1261	1	11.42	0.532	E	40.06
8249-3704	137.8748	45.4683	0.0268	3	10.46	-0.384	SBa	39.05
8329-3701	213.4322	43.6625	0.0893	1	11.08	-0.028	E	38.76
8459-3702	146.7091	43.4238	0.0722	3	11.25	0.736	Sa	39.07
8452-12705	157.9377	46.6717	0.0249	1	10.36	0.323	SABc	37.35
8465-12704	198.1419	48.3666	0.0558	1	10.95	0.019	Sa	39.30
8447-9102	207.4544	40.5374	0.0961	2	11.11	0.338	Sb	39.04
8486-12705	238.1414	46.3399	0.0606	1	11.21	0.213	Sab	38.87
8464-6101	186.1810	44.4108	0.1256	4	11.54	1.446	S0a	40.64
8330-12702	203.8530	38.0952	0.0649	3	10.81	0.670	S0a	38.12
8603-6101	247.1593	39.5513	0.0304	4	11.23	-0.645	E	38.23
8612-12705	255.1016	38.3517	0.0358	2	10.94	0.236	SBa	38.26
8156-12701	54.3896	0.1442	0.0481	4	10.66	-0.947	Sc	36.93
8077-6103	39.4466	0.4051	0.0473	1	10.73	0.093	Sa	38.77
8146-12705	118.0532	28.7726	0.0637	3	11.05	-0.115	SBa	38.37
8714-6102	119.1980	45.8879	0.0561	3	11.29	0.795	SABb	38.93
8711-12701	116.9431	51.6460	0.1009	1	11.34	0.413	S0a	39.63
8720-1901	121.1479	50.7086	0.0227	3	10.11	-1.070	S0	38.35
8952-3703	205.4409	27.1063	0.0288	1	10.53	-0.423	SABbc	37.96
8978-12705	249.5586	41.9388	0.0286	2	10.92	0.509	Sc	38.26
8595-12704	221.2231	51.3411	0.0890	2	11.42	-0.179	E	38.88
8943-9101	156.4031	37.2223	0.0608	4	11.00	0.224	Sa	38.68
8939-12701	124.7068	22.9545	0.0919	1	11.35	-0.043	Sab	39.10
8946-3703	170.5882	46.4305	0.0323	1	10.82	-0.955	S0	38.19
9029-12704	247.2170	42.8120	0.0316	3	10.83	-0.020	SBb	38.47
9039-6102	230.1022	32.8596	0.0620	3	11.26	0.689	Sa	38.60
9036-6102	239.1021	42.3955	0.0408	4	10.93	0.627	Sb	38.67
9047-6104	248.1409	26.3807	0.0586	3	11.39	1.240	Sbc	39.45
8154-9102	45.9602	-0.2045	0.0276	1	10.69	0.655	SBc	38.74
9182-6102	119.4863	39.9934	0.0658	3	11.08	0.243	S0a	39.96
9193-12701	45.9546	-1.1038	0.0136	3	10.87	-0.380	S0a	39.06
8993-9102	165.9101	45.1800	0.0205	3	10.53	-0.452	SABbc	38.70
9491-6102	119.9304	18.4677	0.0378	1	10.22	-1.357	Sb	36.79
9486-9101	120.7992	39.8858	0.0410	1	11.19	-0.516	S0a	38.26
8311-6104	205.2827	23.2821	0.0264	3	10.88	0.876	SABb	39.45
8309-6101	210.1903	51.7287	0.0697	1	11.16	-0.166	Sa	38.53
9507-12704	129.6000	25.7545	0.0182	4	10.67	0.352	S + S	38.74
9507-12705	129.5207	25.3295	0.0282	3	10.63	-0.198	SABb	39.06
9024-12705	223.8675	32.8400	0.0602	2	11.25	0.984	SBbc	38.99
9000-1901	171.4007	54.3826	0.0207	2	10.44	0.524	S0	39.06
9502-9101	128.3419	25.1049	0.0866	1	11.53	0.212	S0	38.95
9502-12703	129.5456	24.8953	0.0287	2	11.15	0.381	SBb	40.00
8985-12703	204.5544	32.8228	0.0245	1	10.51	-0.008	SBc	37.85
9095-6102	243.4418	22.9190	0.0319	1	10.97	0.164	Sab	38.18
9088-9102	242.4723	26.6259	0.0779	4	11.49	0.576	S	38.58
9864-9101	213.9158	50.7138	0.0498	4	10.68	-0.163	Irr	38.22
9870-6103	233.2283	44.5387	0.0371	1	10.80	-0.046	SABA	38.55
9043-3704	230.9032	28.6431	0.0841	1	11.35	-0.290	S0	38.83
9888-3701	236.0080	27.6993	0.0322	3	10.76	0.171	SABA	38.03
9888-12701	235.4758	28.1340	0.0332	3	11.18	-0.257	SBb	38.59
8156-12701	54.3903	0.1448	0.0481	4	10.52	-1.003	Sc	38.31
8322-12702	200.0916	30.4451	0.0476	1	10.96	-0.181	E	38.88
8549-12705	241.9053	45.0655	0.0442	4	10.62	-0.033	Sbc	38.72
8711-12701	116.9417	51.6489	0.1009	1	10.78	0.227	S0a	39.92
8943-9101	156.4018	37.2214	0.0608	4	10.22	-1.382	Sa	39.13
9039-9101	229.0024	34.3553	0.1253	2	10.82	1.116	SABb	40.50
9049-12701	246.6169	24.0270	0.0648	2	11.21	0.302	Sab	38.00
8601-12701	247.7213	41.2863	0.0939	2	9.94	-1.740	S0	39.41

Note. The information of all 61 MaNGA MPL-6 AGNs in galaxy pairs. (1) MaNGA Plate-IFU number; (2) and (3) R.A. and decl. of target galaxy; (4) redshift from MaNGA spectra; (5) merger case classified in Section 2.3; (6) stellar mass in unit of solar mass; (7) star-formation rate; (8) visual morphological classification from MaNGA Visual Morphology Catalogue (https://data.sdss.org/datamodel/files/MANGA_MORPHOLOGY/manga_visual_morpho/) (9) [O III] surface brightness of the central 1''.5 × 1''.5 region.

the 283 MPL-6 AGNs in Comerford et al. (2020), 222 are not in our sample, which consists of 206 (93%) radio (NVSS/FIRST) AGNs with weak or no emission lines, and 16 WISE or

X-ray AGNs. The lack of radio AGNs in our sample indicates that radio AGNs are not necessarily line emitters, as demonstrated in local galaxies (e.g., Best et al. 2005).

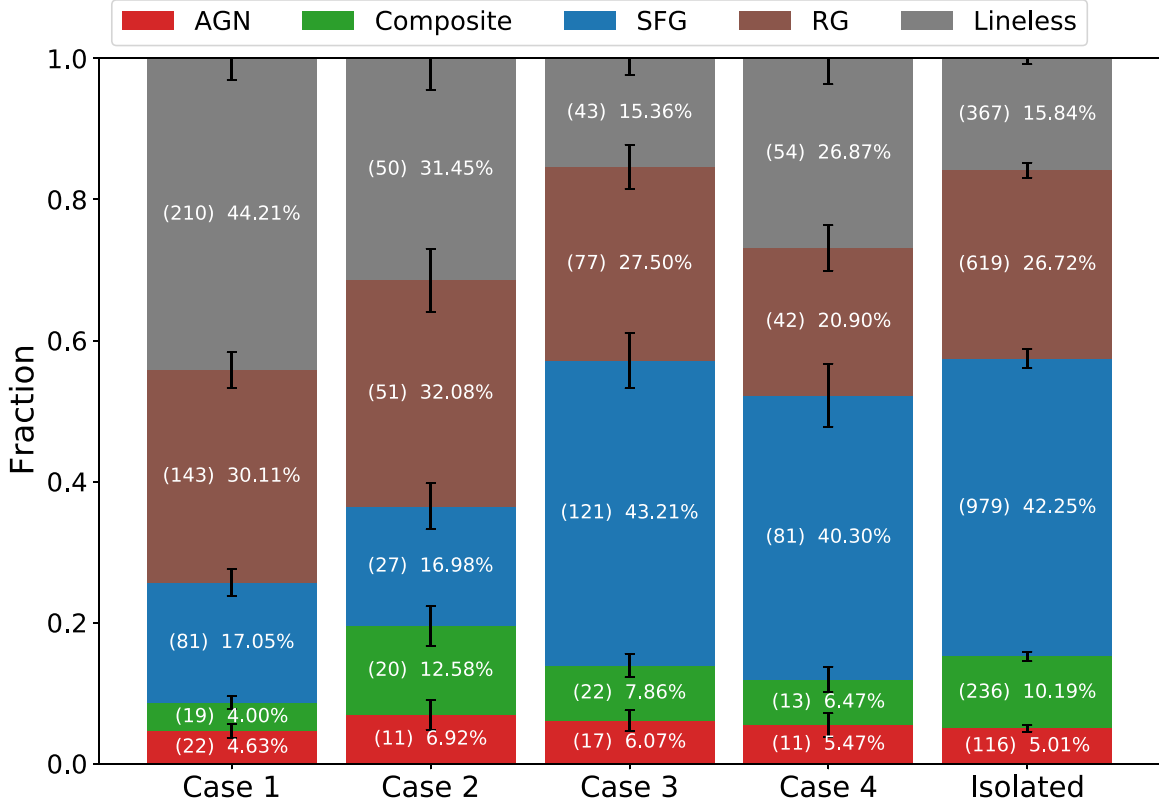


Figure 3. The fractions of the five galaxy types for pairs (in color) in the four merger cases (left four columns, for definition, see Section 2.3) and in isolated galaxies (right panel). In each panel, the colored blocks from the bottom to top represent AGNs (red), composite galaxies (green), SFGs (blue), retired galaxies (RG, brown), and lineless (gray) galaxies, respectively. In brackets are the numbers of galaxies of that specific galaxy type, followed by the percentages in the corresponding cases. The error bars at the top of each color block mark the corresponding binomial errors. Compared to isolated galaxies, no significant difference ($>3\sigma$) in the fraction of galaxy types is found for any merger cases, except for SFG in Cases 1 and 2, and lineless galaxies in Case 1. Overall, higher fractions of passive galaxies (lineless + RGs) by $\sim 15\%-25\%$ are found in Cases 1 and 2.

Table 3
Galaxy Types and Fractions Based on Emission-line Classifications for Different Merger Cases

Case (1)	AGN (2)	Composite (3)	SFG (4)	RG (5)	Lineless (6)	Total (7)
Case 1	4.6% ± 1.0% (22)	4.0% ± 0.9% (19)	17.1% ± 1.9% (81)	30.1% ± 2.5% (143)	44.2% ± 3.1% (210)	475
Case 2	6.9% ± 2.1% (11)	12.6% ± 2.8% (20)	17.0% ± 3.3% (27)	32.1% ± 4.5% (51)	31.5% ± 4.4% (50)	159
Case 3	6.1% ± 1.5% (17)	7.9% ± 1.7% (22)	43.2% ± 3.9% (121)	27.5% ± 3.1% (77)	15.4% ± 2.3% (43)	280
Case 4	5.5% ± 1.7% (11)	6.5% ± 1.8% (13)	40.3% ± 4.5% (81)	20.9% ± 3.2% (42)	26.9% ± 3.7% (54)	201
Isolated	5.0% ± 0.5% (116)	10.2% ± 0.7% (236)	42.3% ± 1.4% (979)	26.7% ± 1.1% (619)	15.8% ± 0.8% (367)	2317
MPL-6	5.3% ± 0.3% (239)	8.4% ± 0.4% (382)	36.2% ± 0.9% (1649)	27.8% ± 0.8% (1267)	22.1% ± 0.7% (1004)	4549

Note. Column 1: Case name, “Isolated” represents these galaxies without a physical companion nor can be identified as merger (see Section 2.3). Columns 2–6: The fraction and its binomial error for each galaxy type in percentage, with the actual number of galaxies (AGN, composite, SFG, retired, and lineless galaxies) listed in brackets. Column 7: The total number of galaxies for each case.

The fractions of each category in different merger cases are listed in Table 3 and shown in Figure 3. Overall, no significant excess or trend in the AGN fractions is found between the four merger cases. Case 1 has the lowest AGN fraction, $4.6\% \pm 1.0\%$, while Case 2 has the highest, $6.9\% \pm 2.1\%$, though in all four cases, the AGN fractions are consistent within 3σ . The AGN fraction in isolated galaxies also has a comparable value of $5.0\% \pm 0.6\%$. Even after including the composite galaxies, the AGN fractions remain more or less constant for the various cases and with the isolated galaxies. Case 2 galaxies, which have the strongest distortion, show higher (AGN + composite) fraction ($19.5\% \pm 3.5\%$), as compared to the isolated galaxies ($15.2\% \pm 0.8\%$). In Cases

1 and 2, we find fewer SFGs ($\sim 17\%$) than in Cases 3 and 4, as well as in isolated galaxies, which have an SFG fraction of $\sim 40\%$. We suspect that this is an environmental effect and will discuss this in more detail in Section 5.2. In Table 3, we also list the total fractions in MPL-6 galaxies for comparison.

On the other hand, we find a clear difference of the fractions of passive (RGs + Lineless) galaxies. Significantly higher fractions ($\sim 15\%-25\%$) of passive galaxies are found in Case 1 ($74\% \pm 4\%$) and Case 2 ($64\% \pm 6\%$), as compared to isolated galaxies ($42\% \pm 1\%$), and $\sim 45\%-50\%$ in Cases 3 and 4. This reflects the selection bias toward more early-type galaxies (ETGs) in Case 1 and Case 2, because ETG pairs hardly show morphological distortions and will be classified as either Case 1

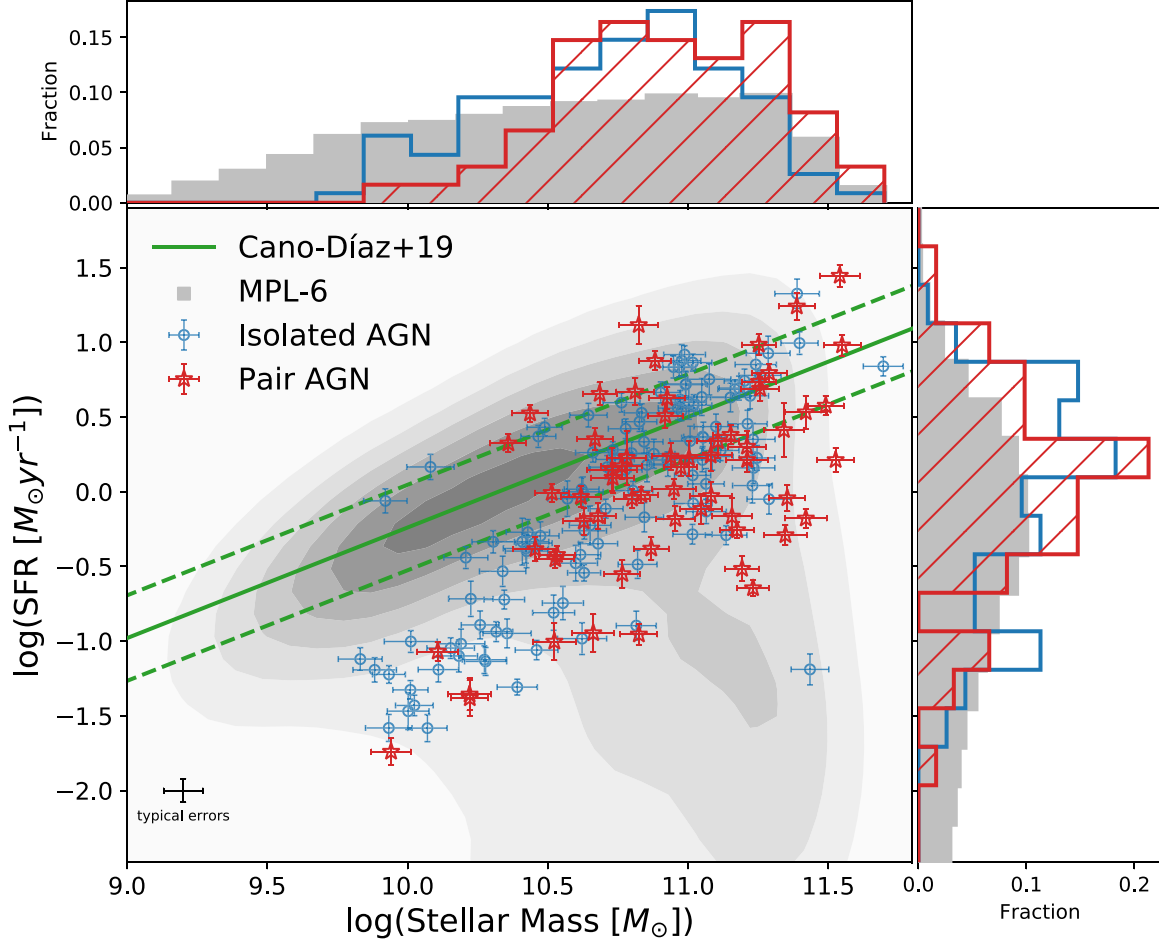


Figure 4. Distribution of M_* vs. SFR for AGNs in our sample (colored stars and circles) and the MaNGA MPL-6 galaxies (gray contour). The contour is generated with a Gaussian-KDE fitting. AGN in isolated galaxies and pairs are plotted as blue circles and red stars, respectively. The solid and dashed green lines are the SFMS and 1σ offset for MaNGA MPL-5 galaxies from Cano-Díaz et al. (2019). Also plotted in the upper and right panels are the normalized distributions of M_* and SFR: gray for all MaNGA MPL-6 galaxies, blue for isolated AGNs, and red for AGNs in pairs. The typical errors are 0.08 dex for SFR and 0.07 dex for M_* . In our sample, AGNs lie mainly on or below the SFMS, which is consistent with Cano-Díaz et al. (2019), and AGNs in pairs tend to have slightly higher SFR and M_* .

(if separated) or Case 2 (if with overlap) based on the criteria in Section 2.3. In addition, we find a higher fraction of passive galaxies in pairs ($60\% \pm 2\%$) than in isolated galaxies ($42\% \pm 1\%$), possibly related to their environments (see Section 5.2 for more discussion).

4. Galaxy Properties

In this section, we present the different galaxy properties of our AGN pair sample, and compare with the control sample of isolated AGNs. We begin with their global properties, including stellar mass, SFR, and central [O III] surface brightness. Then we compare the radial profiles of resolved specific SFR (sSFR), Dn4000, and the Balmer decrement. The H α and [O III] fluxes used in this section are all dust corrected based on the H α /H β flux ratios with a reddening curve ($R_V = 3.1$, gas environment) from Calzetti et al. (2000), assuming the case B recombination ($H\alpha/H\beta = 2.86$, Osterbrock & Ferland 2006). The dust-corrected luminosities of H α and [O III] are calculated using Equation (4):

$$L_{\text{line}} = 4\pi d^2 S_{\text{line}} 10^{0.79 k_\lambda \log(\frac{H\alpha}{2.86 \times H\beta})}, \quad (4)$$

where d is the luminosity distance from the NSA catalog; S_{line} is the observed flux of H α or [O III]; k_λ is the correction factor

from Calzetti et al. (2000), and has a value of 2.4 for H α and 3.5 for [O III].

4.1. The Global Properties

4.1.1. Stellar Mass and Global SFR

The global stellar masses (M_*) and dust-corrected SFRs are taken from the Pipe3D catalog (version 3.0.1). We compare our pair sample with the MaNGA SFMS, based on the Pipe3D results, as defined in Cano-Díaz et al. (2019). In Figure 4, we plot all MPL-6 galaxies (contour) and mark the isolated AGNs as blue circles and AGNs in pairs as red stars. The MPL-6 galaxies show two distinguished populations: one that mainly lies on the SFMS, and another of quenched galaxies that extend to the high mass, low SFR region in Figure 4. All our emission-line-selected MaNGA AGNs have M_* larger than $10^{9.6} M_\odot$. They lie on or below the SFMS, likely in transition between the SFMS and the quenched galaxies, while the less massive AGN hosts appear more quenched. This is consistent with the color-magnitude diagram in Figure 2(d), where most AGN host galaxies are in the “green valley” region. The typical errors are 0.08 dex for SFR and 0.07 dex for M_* .

AGNs in pairs and isolated galaxies are well blended in Figure 4, with no significant difference in SFR (+0.04 dex) or

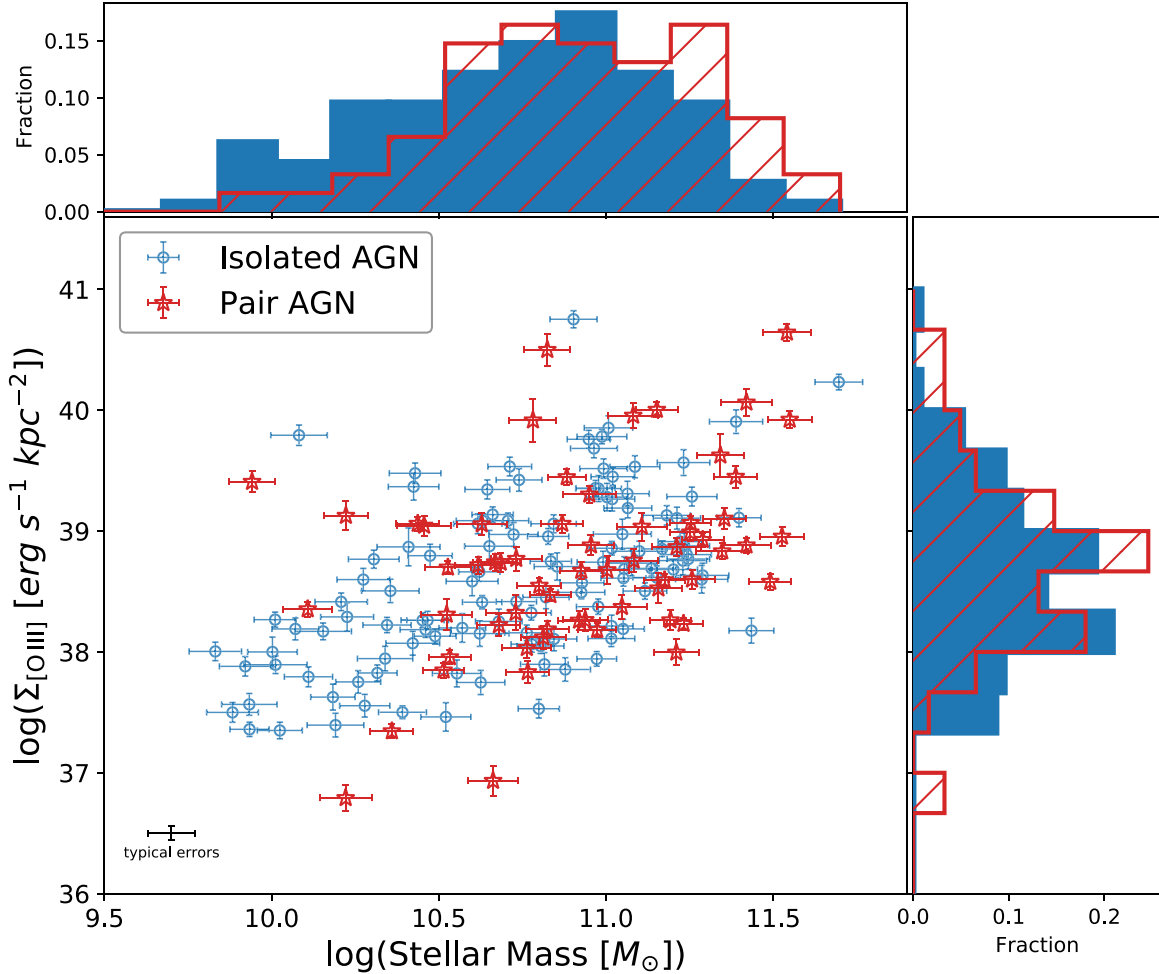


Figure 5. Central [O III] luminosity surface density $\Sigma_{\text{O III}}$ ($1.^{\prime\prime}5 \times 1.^{\prime\prime}5$) vs. global stellar mass for AGNs in MaNGA MPL-6, with red stars for AGNs in pairs, and blue circles for isolated AGNs. Histograms are their normalized distributions and we find marginally higher (+0.13 dex) $\Sigma_{\text{O III}}$ for paired AGNs.

stellar mass (+0.13 dex), though their median SFR ($10^{0.15} M_\odot \text{ yr}^{-1}$) and M_* ($10^{10.93} M_\odot$) are higher than the full MPL-6 sample ($10^{-0.59} M_\odot \text{ yr}^{-1}$ and $10^{10.62} M_\odot$). The lack of low-mass AGN hosts on or above the SFMS may be a combined effect due to the nature of the AGN population as well as the selection effect from the BPT diagnostics. First, the number density of AGN is lower in low-mass host galaxies, as reported in Kauffmann & Heckman (2009), so the limited sample size of the MaNGA survey may miss AGNs in low-mass galaxies. Second, the so-called “star-formation dilution” effect in the BPT diagram is stronger in low-mass, high-SFR host galaxies, as discussed in Trump et al. (2015). We will discuss the AGN selection bias in more detail in Section 3.1.

4.1.2. Stellar Mass and [O III] Surface Brightness

A common proxy for the bolometric luminosity of AGN is the [O III] luminosity (e.g., Heckman & Best 2014). With the IFU data, we only focus on the central [O III], which is dominated by nuclear activity and likely less contaminated from extended SF activities. Same as the BPT classification, we use the central $1.^{\prime\prime}5 \times 1.^{\prime\prime}5$ spaxels to calculate the surface brightness of [O III] ($\Sigma_{\text{O III}} = [\text{O III}] / \text{area}$). We compare the central $\Sigma_{\text{O III}}$ with the global stellar mass distribution in Figure 5. AGNs in pairs have a marginally higher $\Sigma_{\text{O III}}$ than isolated AGNs (+0.13 dex, median error in $\Sigma_{\text{O III}}$ is

0.06 dex). This is different from the result of Liu et al. (2012) using the SDSS single-fiber data. They found a global [O III] luminosity enhancement of 0.5–0.7 dex in AGN pairs. One possible cause of the difference is due to the lack of dust extinction correction in the [O III] luminosity measurements in Liu et al. (2012). As discussed later in Section 4.2.2, in our sample, we found lower Balmer decrement, thus lower extinction correction, in AGNs in pairs than that in isolated AGNs. After the extinction correction, the luminosity difference would be smaller between pairs and isolated galaxies. On the other hand, most of our AGNs have a central $\Sigma_{\text{O III}}$ less than $10^{40} \text{ erg s}^{-1} \text{kpc}^{-2}$, indicating that they are mostly AGNs with moderate luminosities (Kauffmann et al. 2003).

4.2. Resolved Properties

4.2.1. Measurements

To examine the difference between AGN in pairs and isolated galaxies, in this section, we investigate the resolved properties (measured as surface densities Σ_x , in units of $x \text{ kpc}^{-2}$) of the specific SFR ($\Sigma_{\text{SFR}}/\Sigma_{M_*}$), Balmer decrement, and Dn4000, chosen to represent the resolved star formation, dust extinction, and age of the stellar population, respectively.

The mass surface density (Σ_{M_*}) is from the Pipe3D data cube, calculated after fitting the spectra with a model of stellar

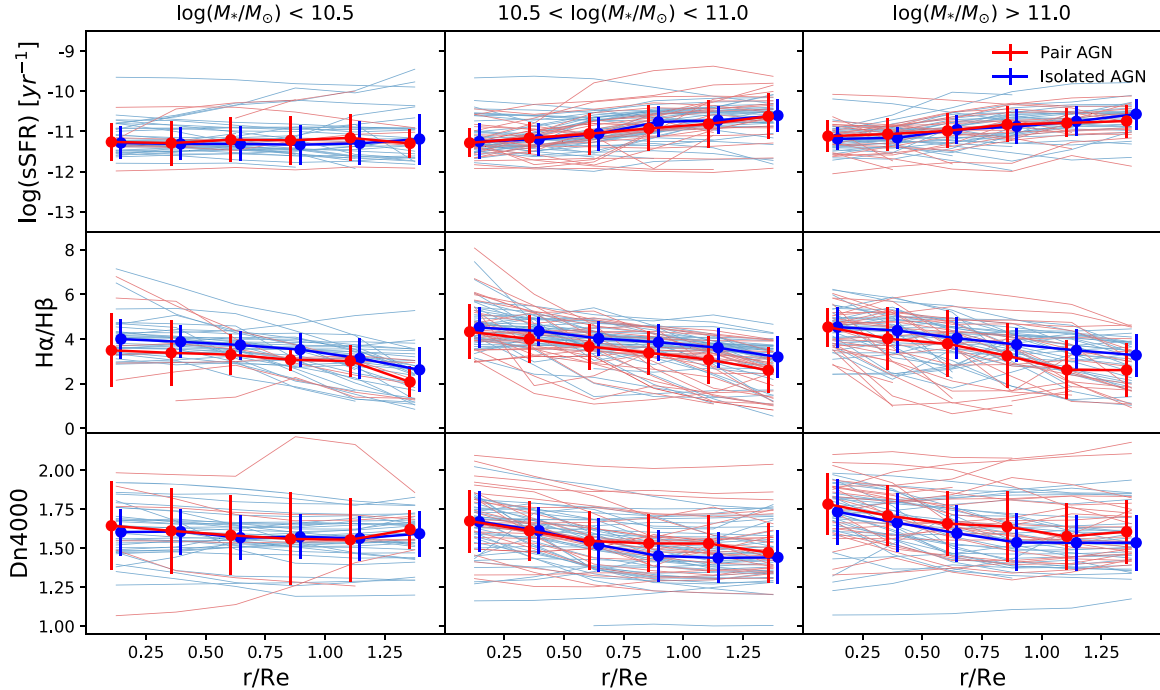


Figure 6. The radial profiles of sSFR (top), Balmer decrement (middle), and Dn4000 (bottom) for AGNs in pairs (red) and isolated AGNs (blue). The AGN sample is divided into three mass bins as listed at the top of each column. The thin lines are the radial profiles for each galaxy in the mass bin. The thick lines with solid dots represent the median value in each radius bin from 0.00 to 1.50 R_e , with a bin size of 0.25 R_e , and manually offset in the x direction to guide the eye. The error bars indicate the 1σ scatter of individual galaxies around the median value. No significant difference is found between AGNs in pairs and isolated AGNs. Both show an increasing sSFR, as well as decreasing Balmer decrement and Dn4000 radial profiles. This is consistent with the inside-out quenching scenario. The only exception is in the low-mass bins ($\log(M_*/M_\odot) < 10.5$), where AGNs show flat sSFR and Dn4000 radial profiles.

populations using the GSF156 single-stellar population library. We obtain the Σ_{SFR} from the attenuation corrected $H\alpha$ luminosity using the star-formation law (Kennicutt & Evans 2012):

$$\log\left(\frac{\text{SFR}}{M_\odot \text{ yr}^{-1}}\right) = \log\left(\frac{L_{H\alpha}}{\text{erg s}^{-1}}\right) - 41.01. \quad (5)$$

This relation is based on the assumption that the $H\alpha$ emission is produced by young stellar populations (e.g., OB stars in H II regions). Therefore, the $H\alpha$ contamination from AGN's NLR will lead to overestimated SFR. We disentangle the AGN's contribution through different line ratios as compared to pure star-forming H II regions.

The intrinsic $[\text{N II}]/H\alpha$ emitted by SF and AGN can be predicted using different photoionization models (e.g., Kewley & Dopita 2002; Groves et al. 2004; Dopita et al. 2013). Ji & Yan (2020) presented a new three-dimensional diagnostic diagram, which can be applied to estimate the contributions from AGN and SF based on a given model. They used the best-fitting SF and AGN model for their MaNGA spaxel sample and derived a relation between AGN's contribution and the indicator P_1 , which can be approximated as Equation (6):

$$f_{\text{AGN}} = \begin{cases} 0, & P_1 \leq -0.53 \\ 0.14P_1^2 + 0.96P_1 + 0.47, & -0.53 < P_1 < 0.51, \\ 1, & P_1 \geq 0.51 \end{cases} \quad (6)$$

where f_{AGN} is AGN's contribution to the $H\alpha$ flux ($H\alpha_{\text{AGN}}/H\alpha_{\text{total}}$) and P_1 equals to $0.63 \log([\text{N II}]/H\alpha) + 0.51 \log([\text{S II}]/H\alpha) + 0.59 \log([\text{O III}]/H\beta)$. We apply this relation to calculate the f_{AGN} of all spaxels with enough S/N (>3), and

then decompose the $H\alpha_{\text{SF}}$ to obtain the SFR through Equation (5). We test this relation for all MaNGA spaxels with robust S/N regardless of their host galaxies' categories in Appendix A.1. Overall the f_{AGN} per spaxel equals to 0 in the star-forming region and increases to 1 toward the edge of the AGN sequence. Thus our SFR corrections will only affect the AGN or composite spaxels, but does not affect SF spaxels, as expected.

The spaxel-by-spaxel Dn4000 and line flux values are from the MaNGA DAP data product. For each galaxy, the effective radius (R_e) is from the NSA catalog and was calculated from the r -band photometry. We then calculate the radial profiles by averaging the corresponding values in six equal radius bins from the center ($0 R_e$) to MaNGA's reliable coverage ($1.5 R_e$) with a bin size of 0.25 R_e .

4.2.2. Radial Profiles

Previous work by Belfiore et al. (2018) showed that the sSFR radial profiles are mass dependent, with low-mass MaNGA main sequence galaxies having higher and more flat sSFR than high mass ones. We first divide all AGN hosts into 3 mass bins of $\log(M_*/M_\odot) < 10.5$, $10.5 < \log(M_*/M_\odot) < 11.0$, and $\log(M_*/M_\odot) > 11.0$. The numbers of AGNs in each mass bin are 32, 64, and 53, respectively. Every galaxies' radial profiles of the sSFR, Balmer decrement, and Dn4000 are shown in Figure 6, with the AGNs in pairs in red and the isolated AGNs in blue. The solid dots and thick lines are generated using the median values in the corresponding radius bins, and the error bars indicate the 1σ scatter of individual galaxies around the median values. The larger uncertainties for

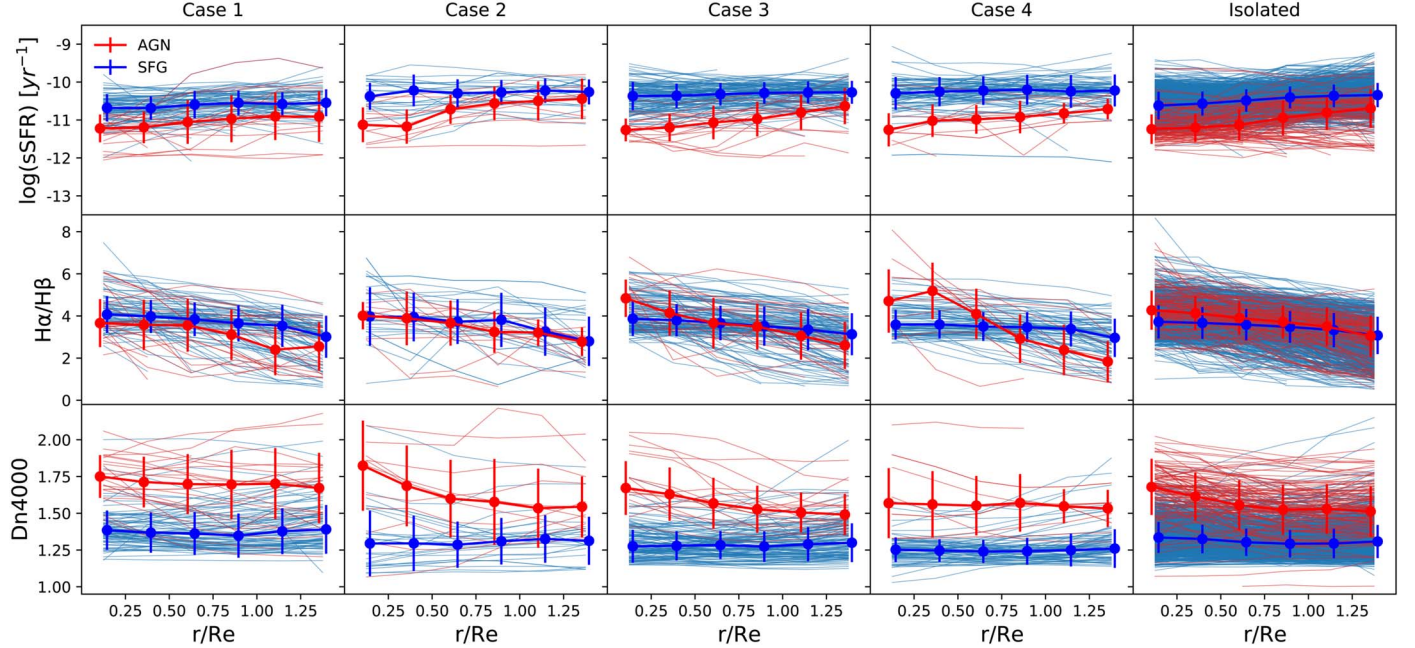


Figure 7. The radial profiles of sSFR, Balmer decrement, and Dn4000, for AGNs (red) and SFGs (blue) divided into different merger cases, and in isolated galaxies. We find no significant evolution along the merger sequence or with the isolated galaxies. Both paired AGNs and SFGs show similar trends with their isolated counterparts. AGNs have an overall increasing sSFR, decreasing Balmer decrement and decreasing Dn4000 as the radius increases, while the SFGs have overall flat sSFR and Dn4000 radial profiles. This suggests that AGNs are more quenched and have older central stellar populations than SFGs, regardless if they are in pairs or in isolated galaxies. The total galaxy numbers for each subsample are listed in Table 3.

AGNs in pairs are related to the relatively smaller sample size. From the radial profiles, we observe that:

- The sSFR radial profiles show no significant difference between AGNs in pairs or isolated AGNs in all mass bins. In the lowest mass bin ($\log(M_*/M_\odot) < 10.5$), AGNs in pairs have a flat sSFR radial profile. At $\log(M_*/M_\odot) > 10.5$, both AGNs in pairs and isolated galaxies have an increasing sSFR toward larger radius, indicating an inside-out quenching.
- The Balmer decrements decrease from the inside to the outside, indicating more dust attenuation in the nuclear region. As in the case of sSFR, the Balmer decrement is also flatter in the lowest mass bin for AGN in pairs, but not as flat as the sSFR and Dn4000 in the same mass bin. AGNs in pairs tend to have lower Balmer decrements than isolated AGNs, though not significant ($<1\sigma$).
- Overall, the Dn4000 radial profiles decrease toward larger radii, indicating younger stellar populations in the outer regions of the galaxy. Again, this trend is less obvious in low-mass AGNs, which is consistent with the flatter trend of sSFR radial profiles (top panel).
- For all AGN host galaxies more massive than $10^{10.5} M_\odot$, the radial profiles of the sSFR, Balmer decrement, and Dn4000 do not change as the stellar mass increases. At the lowest mass bin ($M_* < 10^{10.5} M_\odot$), however, the radial profiles of the AGN, regardless in pairs or isolated galaxies, show flatter sSFR with lower absolute values, and flatter Dn4000 profiles, which is again consistent with the inside-out picture. These results are different from similar analysis for SFGs. Elevated sSFRs are found in the SFG pairs regardless of their mass values, especially in the nuclear region (e.g., Pan et al. 2019; Steffen et al. 2021). Higher sSFR are found in low-mass

SFGs (e.g., Belfiore et al. 2018), which is opposite to what we find in our AGN host galaxies.

Figure 7 shows the similar radial profiles as Figure 6, except that galaxies are separated by their merger cases, with red and blue lines represent the AGNs and SFGs, respectively. For AGNs, the overall sSFR radial profile is increasing, consistent with the declining Dn4000 radial profiles, and their trends indicate a centrally depressed SFR along older stellar populations, suggesting more quenched nucleus regions. The Balmer decrement radial profiles also decrease from the inside to the outside, indicating more dust attenuation in the central region. From Case 1 to Case 4, the radial profiles of these parameters do not show any significant evolution. Central Balmer decrements are slightly higher in Cases 3 and 4, consistent with the scenario of dustier later merger stages. On the other hand, SFGs show clearly higher and flatter sSFR radial profiles, similar Balmer decrement radial profiles, and lower and flatter Dn4000 radial profiles than AGNs, both pairs and isolated galaxies. These findings are consistent with the star-forming nature of the SFGs, which have ongoing star formation both in the nucleus and the outskirts. We will discuss the difference between the AGN and SFG radial profiles in more detail in Section 4.3.

4.3. Comparison to Star-forming and Passive Galaxies

In this section, we compare the differences among AGNs, SFGs, and passive galaxies. Similar to Section 4.2.2, we calculate the radial profiles of each galaxy and use the median value to generate the stacked profiles in Figure 8. Here the shadowed errors are obtained by calculating the standard deviation divided by \sqrt{N} , where N is the number of values at each radius bin.

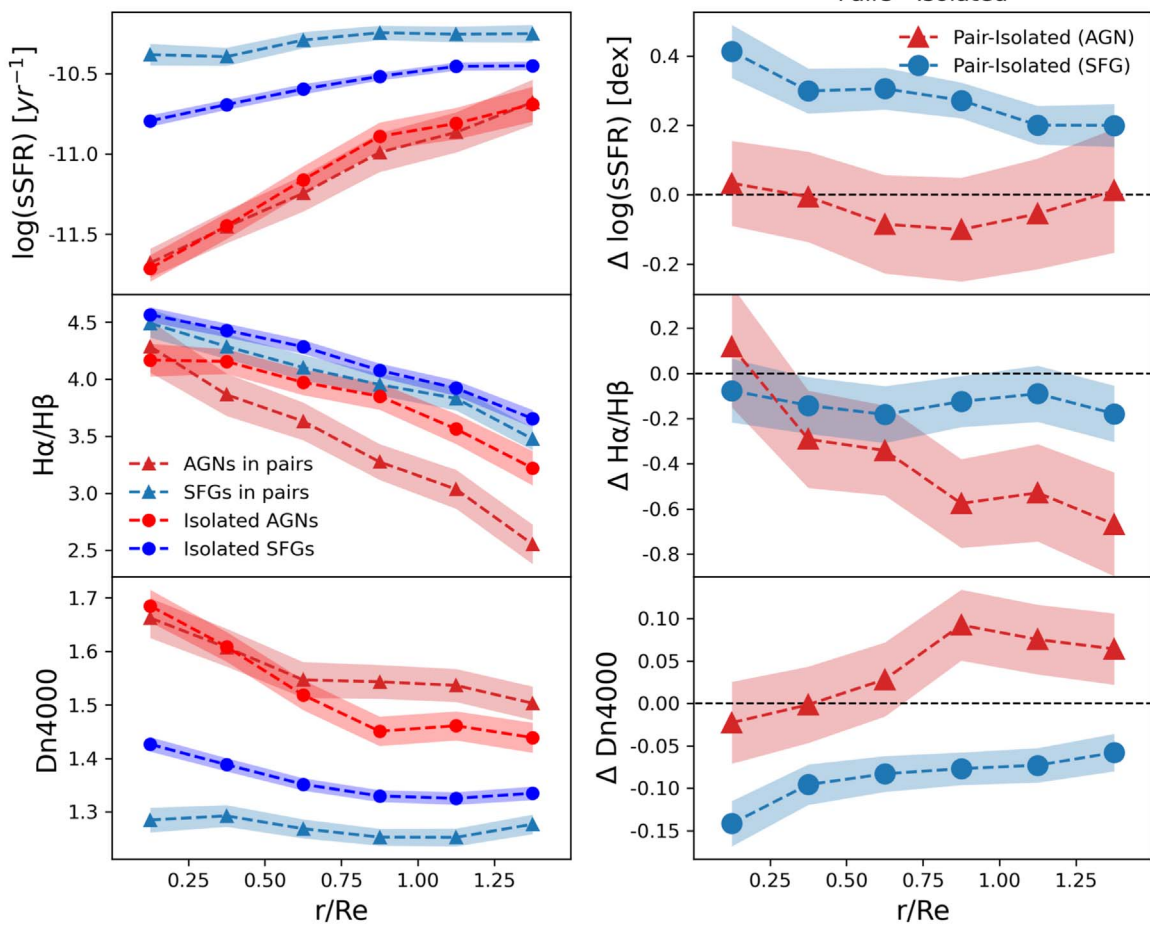


Figure 8. Comparison of the radial profiles between mass-controlled AGNs (red) and SFGs (blue). From top to bottom: the sSFR, Balmer decrement, and Dn4000 as a function of radius for AGNs and SFGs in pairs (triangles) and isolated ones (dots). Left panel shows the absolute values and the right panel shows the difference between pairs and isolated galaxies. The shadows represent the standard deviation of the mean at each radius bin. AGNs have lower sSFR and higher Dn4000 at all radii, regardless of whether they are in pairs or isolated galaxies. Unlike SFGs in pairs, which show enhanced sSFR and suppressed Dn4000 toward the galaxy center, AGNs do not show any significant difference in the radial profile between pairs and isolated ones.

Using the mass-controlled subsamples defined in Section 2.4, we first compare the resolved properties between AGNs and SFGs. The radial profiles of SFGs and AGNs in both pairs and isolated galaxies are shown in the left panel of Figure 8. In both galaxy pairs and isolated galaxies, SFGs have higher sSFR and lower Dn4000 values than AGN hosts at all radii, and have flatter radial profiles. This indicates more star formation and younger stellar populations in SFGs, as expected. AGNs (red triangle and circles in Figure 8, left) have lower sSFR and higher Dn4000 values in the central regions, consistent with the “inside-out” quenching scenario. For the Balmer decrement radial profiles, we find that the absolute value is almost the same in the center for AGNs and SFGs, but decreases faster in AGNs toward the outskirts, especially for AGNs in pairs. This is consistent with the more dusty outskirts in SFGs.

We further compare the differential radial profiles for pairs and isolated galaxies in the right panel of Figure 8. Compared to isolated SFGs, SFGs in pairs show clearly enhanced sSFR and suppressed Dn4000, which is more obvious in the central regions, consistent with previous findings (e.g., Pan et al. 2019; Steffen et al. 2021). Compared to paired AGNs, isolated AGNs have a marginally increasing sSFR toward the larger radii.

The Balmer decrement is almost the same in paired and isolated SFGs, but decreases in AGNs from the center to the outskirts, with $\Delta(\text{H}\alpha/\text{H}\beta)$ dropping from 0 to -0.6 . We note that other than different dust attenuation, the intrinsic $\text{H}\alpha/\text{H}\beta$ value can also vary in different regions of a galaxy due to different interstellar medium (ISM) environment. For example, higher temperature or higher electron density can also result in lower Balmer decrements (Osterbrock & Ferland 2006). Thus we refrain ourselves from over-interpreting the trend in the Balmer decrement.

We make similar comparison with the passive galaxies in Figure 9, with a mass-controlled passive subsample as defined in Section 2.4. Given the low S/N of $\text{H}\alpha$ and other emission lines, it is difficult to derive the SFR of most spaxels in the passive galaxies. Dn4000 (or D4000) has been used to study the SFR in passive galaxies, by using single-fiber spectra (e.g., Brinchmann et al. 2004; Salim et al. 2007; Rosario et al. 2016), or IFU spectra (e.g., Spindler et al. 2018; Wang et al. 2019; Bluck et al. 2020). Inspired by this, we derive our own resolved sSFR vs Dn4000 relation, using the MaNGA spaxels with robust $\text{H}\alpha$ -based sSFR in all MPL-6 galaxies (Appendix A.2). Since Balmer decrements are not reliable in spaxels with low S/N of $\text{H}\alpha$ and $\text{H}\beta$ or no emission lines, in Figure 9 we only

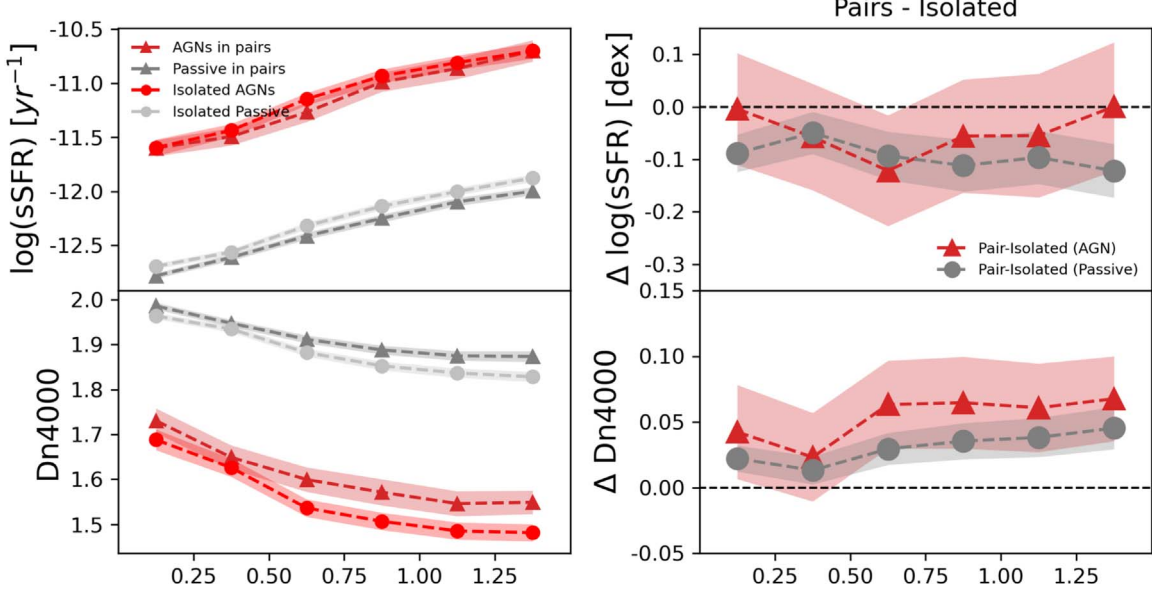


Figure 9. Comparison of the radial profiles of the sSFR (top) and Dn4000 (bottom) between the mass-controlled AGNs (red) and passive galaxies (gray). Galaxy in pairs are marked with triangles, and isolated ones in dots. The sSFR of passive galaxies is calculated by the Dn4000-sSFR relation described in Appendix A.2. AGNs have higher sSFR and lower Dn4000 at all radii than isolated galaxies, regardless of whether they are in pairs or isolated. No difference is found between the isolated galaxies and galaxies in pairs. The total galaxy numbers for each subsample is listed in Table 1.

compare the sSFR and Dn4000 radial profiles of the passive galaxies with AGNs.

The radial profiles of AGNs and passive galaxies show similar declining sSFR trends as radius decreases (Figure 9, left), consistent with the inside-out quenching scenario. Regardless of the similar trends, passive galaxies still have lower sSFR by ~ 1.2 dex, and higher Dn4000 by ~ 0.3 . This indicates that AGN host galaxies, despite having lower sSFR than the SFGs (Figure 8), are still not as quenched as passive galaxies. AGNs are more likely in transition between SFG and passive galaxies. Comparing isolated and paired passive galaxies, we find no difference with AGNs in their $\Delta \log(\text{sSFR})$ and $\Delta Dn4000$ (Figure 9, right). The differential radial profiles between AGN and passive galaxies are generally flat within 3σ , suggesting no interaction-triggered star-formation activities in both populations.

In summary, unlike SFGs, AGNs and passive galaxies in pairs do not show SFR enhancement as compared to isolated galaxies. One explanation of the less impact on star formation in AGN hosts may be the lack of sufficient gas, similar to the passive galaxies.

5. Discussions

5.1. Comparison to Previous Studies

Several previous works using single-fiber spectra from large surveys have found no AGN fraction evolution based on BPT-selected AGNs among different galaxy merger cases. These studies found the same AGN fraction in galaxy pairs and isolated control sample (e.g., Schmitt 2001; Coldwell & Lambas 2006; Alonso et al. 2007; Ellison et al. 2008; Darg et al. 2010), no enhanced [O III] luminosity in AGNs within galaxy pairs (e.g., Li et al. 2008b), and no increase in neighbor numbers for higher [O III] luminosity AGNs (e.g., Shao et al. 2015). Our sample is the first to study AGN fractions along the merger sequence based on IFU data, and we find no change of

the IFU-classified AGN fraction for different merger cases and isolated galaxies.

On the other hand, using galaxy pair samples from the IFU surveys, Barrera-Ballesteros et al. (2015a), Thorp et al. (2019), Pan et al. (2019), and Steffen et al. (2021) have studied the spatially resolved sSFR of SFGs in pair or merger systems. Despite the different sample selections, a unanimous conclusion is that, in SFGs, galaxy interactions trigger stronger SF enhancements in the center than in the disk. The radial profile of the SFGs in our sample is also plotted in Figure 8 and is consistent with previous studies with higher SF enhancement in the center. The AGNs in pairs, however, do not show any SF enhancement as compared to isolated AGNs. Pan et al. (2019) perform the analysis along the merger sequence and found the enhancement evolves in different merger cases. The enhancement of central sSFR emerges after the “pre-merger” phase (Case 1). We use the same parent pair sample and focus on the AGN pairs. We find that unlike SFGs, the evolution of AGNs’ properties along the merger sequence is not statistically significant (Figure 7).

The global and resolved properties of our AGNs are in general agreement with an inside-out quenching scenario, as proposed in several earlier MaNGA works. Compared to that in outer regions, the decrease of SFR in the central regions contributes more to galaxy quenching (e.g., Ellison et al. 2018; Pan et al. 2018; Guo et al. 2019). Based on our AGNs’ GV-like colors (Figure 2, (d)), location below the SFMS (Figure 4), and sSFR and Dn4000 radial profiles being in between the SFGs and the passive galaxies (Figures 8, 9), our BPT-selected AGNs are likely to be experiencing the transition from SFGs to quiescent galaxies. The locations on the main sequence and the color-magnitude diagram of our AGN sample are similar to previous BPT-selected AGNs in MaNGA (Fu et al. 2018; Sánchez et al. 2018). This possible transition can be explained by gas consumption, by either previous star formation, or AGN triggered outflows. If the gas has been consumed already in the AGN systems, then the lack of sSFR enhancement in AGN

samples, as observed in our sample, can be naturally explained. This is also supported by the lower global gas fractions than SFGs found in MaNGA AGNs (e.g., xCOLD GASS survey, Saintonge et al. 2017), and lower H₂ mass in AGNs than normal SFGs at comparable star-formation efficiencies (Lin et al. 2017).

5.2. Selection Bias from the Environment

In Section 3.2, we find a higher fraction of passive galaxies in pairs. It is known that massive, bright, and passive early-type galaxies tend to locate in a dense, clustering environment (e.g., Zehavi et al. 2005; Li et al. 2006; Skibba et al. 2009; de la Torre et al. 2011). In this section, we discuss the environmental influence on our MaNGA pair sample.

Different environmental indicators such as neighboring galaxies and halo occupation distribution represent the galaxy environment at different scales (see Muldrew et al. 2012 for a review). Previous work by Kauffmann et al. (2004) has shown that star formation mainly depends on galaxies' local environment. Here we adopt the local mass density (ρ) from the MaNGA-GEMA¹² catalog to investigate the influence of the galaxy environment. The local mass density uses the halo-domain method developed by Wang et al. (2009) for the SDSS DR7 galaxy group catalog (Yang et al. 2007), which reconstructs the cosmic density field by calculating the Gaussian-kernel smoothed density at each galaxy's position on a scale of 1 Mpc/h. We compare the galaxy fraction for different galaxy types (lineless + RG, SFG + composite, and AGN) with their local mass densities (Figure 10). The local mass densities are divided into four bins: $\log(\rho/\rho_0) = (-\infty, 0]$, $(0, 0.9]$, $(0.9, 1.3]$, and $(1.3, +\infty)$, where ρ_0 , the average cosmic mean density, is $7.16 \times 10^{10} M_\odot h^{-1} (\text{Mpc}/h)^{-3}$. The fraction of passive galaxies increases with the local mass density bin from $25\% \pm 2\%$ ($\log(\rho/\rho_0) < 0$) to $69\% \pm 3\%$ ($\log(\rho/\rho_0) > 1.3$). This is consistent with the observations that passive galaxies tend to locate in a denser environment (e.g., Norberg et al. 2002). In contrast, the fraction of SFG + composite galaxies decreases as the local density increases (e.g., Kauffmann et al. 2004; Coil et al. 2017). The AGN fraction remains more or less the same from the lowest density ($3.9\% \pm 0.7\%$) to the highest density ($5.6\% \pm 0.9\%$), with a peak ($7.6\% \pm 1.2\%$) at the median density of $\log(\rho/\rho_0) = 0.9-1.3$.

We have shown that the more passive MaNGA galaxies live in denser environments, we then compare the local mass density distributions between isolated galaxies and paired galaxies. In Figure 11, we plot the $\log(\rho/\rho_0)$ distribution for our four cases, along with the differences of the mean density in pairs and isolated galaxies. The distribution of $\log(\rho/\rho_0)$ is clearly higher for galaxies in Case 1 and Case 2 pairs, as compared to isolated galaxies (+0.63 dex, +0.45 dex, respectively). The density distributions in Case 4 are more similar with the isolated galaxies, with $\Delta \log(\rho/\rho_0)$ of +0.07 dex only. We suspect that our observed higher fractions of passive galaxies in Case 1 and Case 2 are a result of their overall denser environment. The lack of a significantly higher fractions of passive galaxies in Case 3 is a result of the morphology-based case definition, which excludes ETGs from Case 3 classification, as discussed in Section 3.2.

¹² https://data.sdss.org/datamodel/files/MANGA_GEMA/GEMA_VER

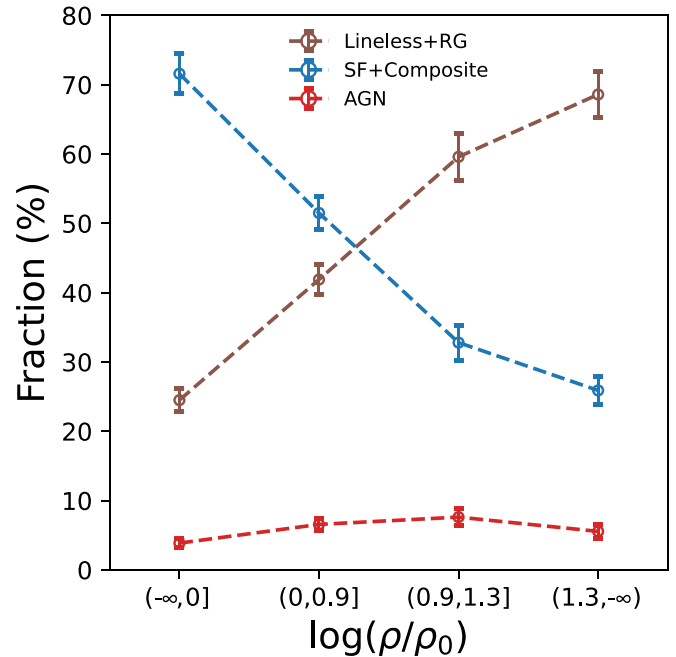


Figure 10. Fractions of isolated galaxies dividing into four local density bins. Error bars represent the binomial errors of each fraction. The parameter ρ_0 , the average cosmic mean density, equals $7.16 \times 10^{10} M_\odot h^{-1} (\text{Mpc}/h)^{-3}$. The passive fraction becomes higher and the (SFG + composite) fraction becomes lower in denser environment, but the AGN fraction does not change significantly. The total numbers for each galaxy type can be found in Table 3.

5.3. Selection Bias of the AGN Sample

In this paper, we use optical emission-line ratio and line width to select AGNs. This method is based on the different emission-line properties in AGNs' NLRs and H II regions. The emission from NLR could be contaminated by the broad emission lines or strong nuclear starbursts. Therefore, our BPT selection is biased against AGNs with a strong broad-line component or with strong central star formation (e.g., Trump et al. 2015). The AGNs missed due to dust extinction or dilution from star formation are known to lie along or above the SFMS (e.g., Chang et al. 2017), which possibly contributes to the lack of AGNs above the SFMS in our Figure 4. Another selection bias of the BPT method is against AGNs with quenched host galaxy that has no or weak emission lines due to lack of recent star formation (e.g., Heckman & Best 2014). For instance, radio-selected AGNs are doomed to be left out in our sample (e.g., the majority of radio AGNs have no emission lines from Comerford et al. 2020, see Section 3.1). In addition, the MaNGA survey aims to study the resolved properties of nearby galaxies. The most luminous quasars are therefore not a preferred target as they easily outshine the host galaxies, making the data analysis difficult (Wake et al. 2017). As a result, our sample is biased toward AGNs with median to low luminosity and low SFR, landing them in the transition region in Figure 4.

5.4. Caveats in the Analysis of Mergers

When it comes to the late stage of merging, there are several caveats in both sample selection and the analysis. The first caveat is the merger classification. As mentioned in Section 2.2, we visually classify the late-stage merger systems missed by the pair selection based on physical separation and

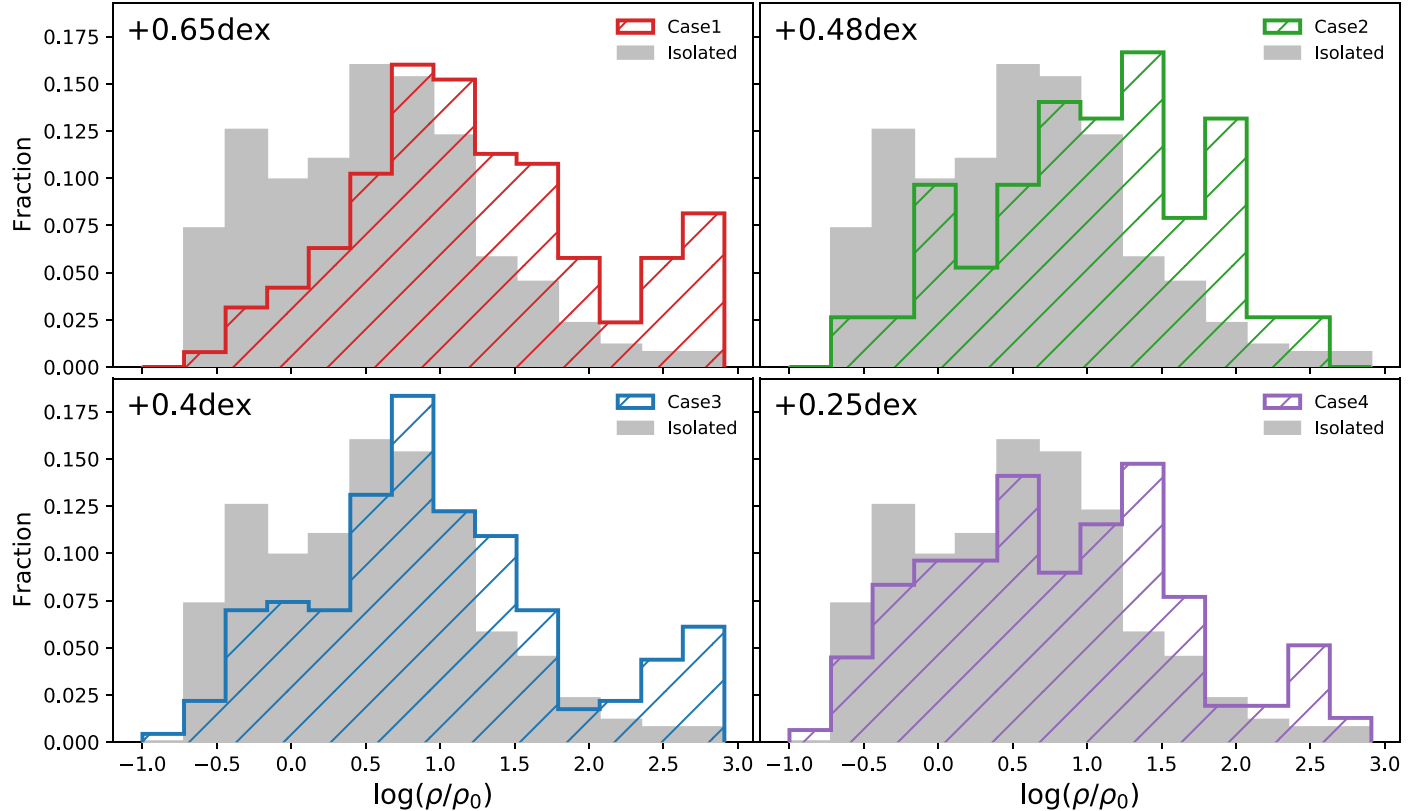


Figure 11. Histograms of the local mass density for galaxies in four merger case and isolated cases. The distribution offsets are listed in the top left of each panel. Case 1 and Case 2 show clearly higher local density distributions than isolated galaxies. The actual numbers for each pair case can be found in Table 3.

velocity offset. Mergers with high inclination would be missed, while secularly evolved irregular galaxies could also contaminate the merger sample. In addition, some galaxy pairs may not follow the Toomre Sequence (Toomre & Toomre 1972) and should not be included in merger-sequence-related analysis. For example, Sinha & Holley-Bockelmann (2012) have simulated and found that there are at least 20%–30% flybys in galaxy pair samples from large surveys, which may smear out the actual evolutionary trends of the true merging pairs.

Moreover, the distortions in galaxy pairs may affect our analysis of their host galaxies. The radii generated from typical ellipsoid model may not be appropriate for galaxies with bridges or tails, resulting in inaccurate R_e estimate. The overlapping region between galaxies may contaminate the measurements of their properties. Last, even though we require our isolated control sample to show no distortion in SDSS images and have no spectroscopic companion, it is possible that their SFR are affected by hidden minor mergers or flybys.

6. Summary

In this work, we select 1156 local galaxies in pair or merger systems from the MaNGA MPL-6 and classify them into four categories (cases), presumably representing various stages along the merger sequence. Then we identify 61 AGNs in these pair systems using the BPT and WHAN diagrams and compare them with isolated AGNs and SFGs via both global and resolved properties. We calculate the AGN fractions along the merger sequence, analyze their global SFR- M_* relation, Σ [O III], and their resolved radial profiles of the sSFR, Balmer decrement, and Dn4000. Our main conclusions are as follows:

- (1) The AGN fraction of galaxies in pair or merger systems is consistent with that in isolated galaxies ($\sim 5\%$). This in agreement with several previous SDSS works that found no significant AGN fraction change in galaxy pairs (e.g., Alonso et al. 2007; Ellison et al. 2008; Darg et al. 2010). Besides, we do not find any evolution in AGN fractions for the different merger cases. More passive galaxies and fewer SFGs are found in galaxy pairs, especially in early merger stages, possibly due to their denser environment.
- (2) As for the global properties, AGNs tend to locate in the transition region between main sequence galaxies and passive galaxies, partly due to selection bias. Compared to isolated AGNs, AGNs in pairs have similar stellar mass, global SFR, and Σ [O III].
- (3) The resolved sSFR of AGN host galaxies, whether in pairs or isolated, show an increase from the center to the outskirts. This supports the “inside-out” quenching scenario in AGN host galaxies. Unlike the higher mass AGNs, AGNs with lower stellar mass ($\log(M_*/M_\odot) < 10.5$) show a different sSFR radial profile that is flat across all radii. We find no sSFR difference between AGNs in pairs and isolated AGNs.
- (4) The Balmer decrements of AGN host galaxies show an inside-out decrease, indicating more dust attenuation in the central regions.
- (5) The Dn4000 radial profile for AGNs decreases from the center to the outskirts, and suggests older stellar populations in the galaxies’ central regions with no recent star formation, which is consistent with the sSFR results, and similar to quenched galaxies reported earlier. AGNs with lower stellar mass ($\log(M_*/M_\odot) < 10.5$)

- show a different Dn4000 radial profile that is flat across all radii.
- (6) At all radii, AGNs have significantly lower sSFR and higher Dn4000 than SFGs, regardless of whether they are in pairs or isolated galaxies. They also show steeper Balmer decrement radial profiles. The enhanced SF in SFG pairs are not found in AGN pairs. Galaxy interactions enhance the sSFR of SFGs at all radii, especially in the central region, resulting in higher sSFR and lower Dn4000. While in AGNs and passive galaxies, no significant change in sSFR or Dn4000 is found between pairs and isolated galaxies.

We thank the anonymous referee for their helpful comments that helped improve the presentation of the paper. We also thank Kevin Xu, Nicholas Fraser Boardman, Chuan He, and Zijian Li for helpful discussions. Support for this work is provided by the Chinese National Nature Science Foundation grant No. 10878003. This work was supported in part by the National Key R&D Program of China via grant No. 2017YFA0402703 and by NSFC grants 11433003, 11822303, 11773020, 11733002, 11933003, 11373034, 11803044, and 11673028. Additional support came from the Chinese Academy of Sciences (CAS) through a grant to the South America Center for Astronomy (CASSACA) in Santiago, Chile. This project makes use of the MaNGA-PIPE3D data products, and we thank the IA-UNAM MaNGA team for creating this catalog, and the CONACyT-180125 project for supporting them.

Funding for the Sloan Digital Sky Survey IV has been provided by the Alfred P. Sloan Foundation, the U.S. Department of Energy Office of Science, and the Participating Institutions. SDSS-IV acknowledges support and resources from the Center for High-Performance Computing at the University of Utah. The SDSS website is www.sdss.org. SDSS-IV is managed by the Astrophysical Research Consortium for the Participating Institutions of the SDSS Collaboration including the Brazilian Participation Group, the Carnegie Institution for Science, Carnegie Mellon University, the Chilean Participation Group, the French Participation Group, Harvard-Smithsonian Center for Astrophysics, Instituto de Astrofísica de Canarias, The Johns Hopkins University, Kavli Institute for the Physics and Mathematics of the Universe (IPMU)/University of Tokyo, the Korean Participation Group, Lawrence Berkeley National Laboratory, Leibniz Institut für Astrophysik Potsdam (AIP), Max-Planck-Institut für Astronomie (MPIA Heidelberg), Max-Planck-Institut für Astrophysik (MPA Garching), Max-Planck-Institut für Extraterrestrische Physik (MPE), National Astronomical Observatories of China, New Mexico State University, New York University, University of Notre Dame, Observatório Nacional/MCTI, The Ohio State University, Pennsylvania State University, Shanghai Astronomical Observatory, United Kingdom Participation Group, Universidad Nacional Autónoma de México, University of Arizona, University of Colorado Boulder,

University of Oxford, University of Portsmouth, University of Utah, University of Virginia, University of Washington, University of Wisconsin, Vanderbilt University, and Yale University.

Software: astropy (Astropy Collaboration et al. 2013), Marvin (Cherinka et al. 2019).

Appendix A SFR in AGNs and Passive Galaxies

A.1. Decomposition of the H α Emission

In this Appendix, we describe how we do the AGN-SF decomposition of the dust-corrected H α , as mentioned in Section 4.2.1. We require that the S/N of [O III] $_{\lambda 5007}$, H β , [N II] $_{\lambda 6584}$, H α , and [S II] $_{\lambda\lambda 6716,6731}$ all be greater than 5. We use these emission lines and Equation (6) to calculate the contribution of AGN to H α emission ($H\alpha_{AGN}/H\alpha_{total}, f_{AGN}$). Then we plot all the qualifying spaxels in the BPT and modified BPT diagrams, as shown in Figure A1, coded by their f_{AGN} values. In the star-forming regions of the two diagrams, the AGN's contribution to H α emission is negligible. Along the Ke01 maximum starburst line (black dashed) in the [N II]-BPT diagram, the f_{AGN} is about 40%, consistent with the approximation ($\sim 50\%$) in Kauffmann & Heckman (2009), derived from the SDSS single-fiber spectra. The 100% AGN boundary is better defined in the [S II]-BPT diagram than that in the [N II]-BPT diagram.

A.2. The sSFR-Dn4000 Relation

For MaNGA spaxels with low S/N or without H α emission, SFR cannot be derived directly from the H α emission. Inspired by Spindler et al. (2018), Wang et al. (2019), and Bluck et al. (2020), here we adopt Dn4000 as a proxy of sSFR. We derive the sSFR-Dn4000 correlation based on all MPL-6 spaxels with robust stellar mass, dust-corrected H α luminosity, and Dn4000 values, regardless of their galaxy type. Figure A2 shows the actual distribution of the reliable Dn4000 and sSFR distributions for all spaxels, and the derived median and 1σ dispersion, with a Dn4000 bin size of 0.05. The fifth-order polynomial fit can be expressed as $y = 19.0x^5 - 145.0x^4 + 473.5x^3 + 651.9x^2 + 478.1x - 147.6$, where $y = \text{sSFR}$, and $x = \text{Dn4000}$. The average 1σ dispersion for sSFR is ~ 0.6 dex. We note that this function can only be used in the Dn4000 range between 1.0 and 2.1. Our derived correlation shows a similar negative trend as found in previous works, though the gradient factor and uncertainties vary from study to study. The difference may rise from the different SFR estimators used. For instance, single-fiber H α luminosity was used in Brinchmann et al. (2004), while UV photometry was used in Salim et al. (2007), and IFS H α luminosity in Spindler et al. (2018), Wang et al. (2018), and Bluck et al. (2020). Here we use the dust-corrected, AGN-removed IFU H α for each spaxel.

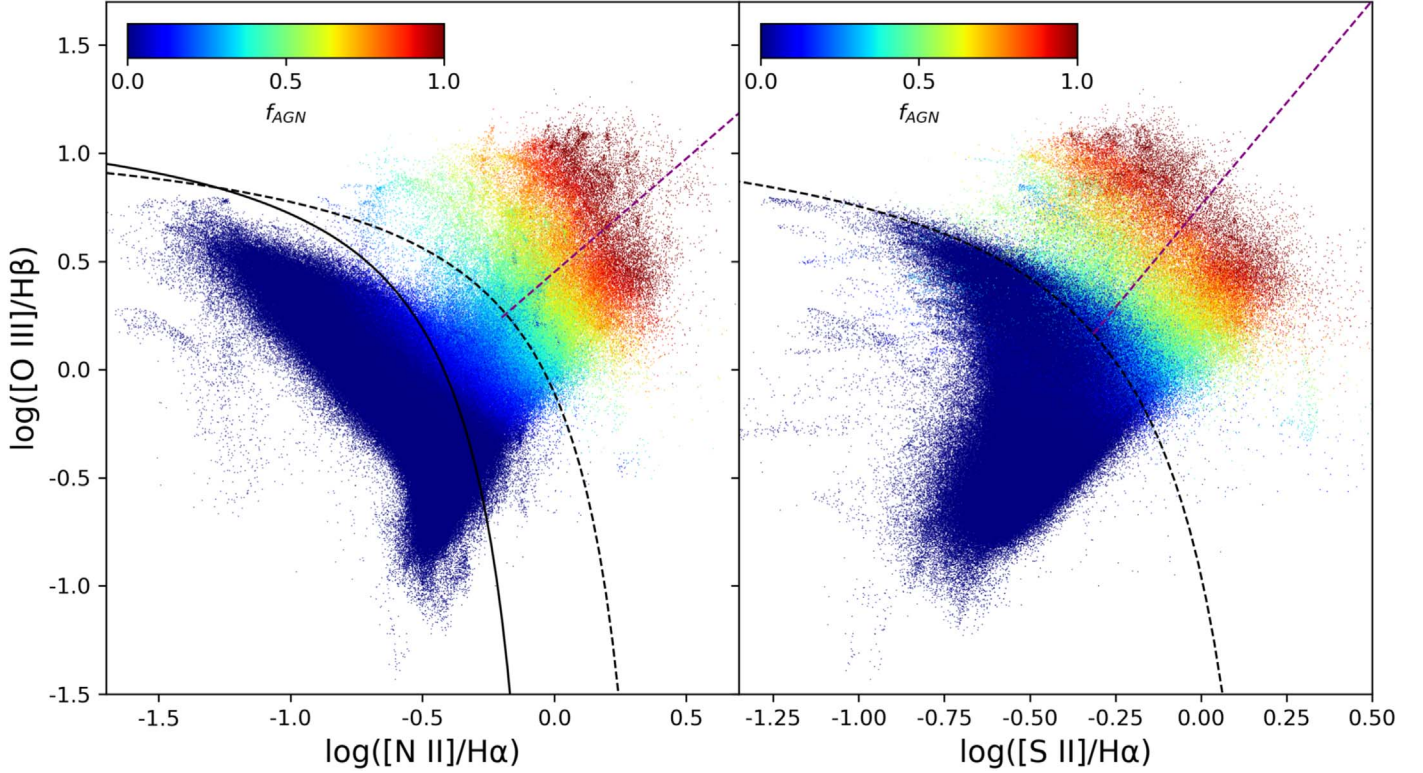


Figure A1. Spaxels' location in the BPT diagrams and their AGN fraction to the H α emission (f_{AGN}). All spaxels have robust S/N and are coded by the value of f_{AGN} derived from Equation (6). The f_{AGN} increase from 0 in the star-forming region to 1 toward the edge of AGN sequence.

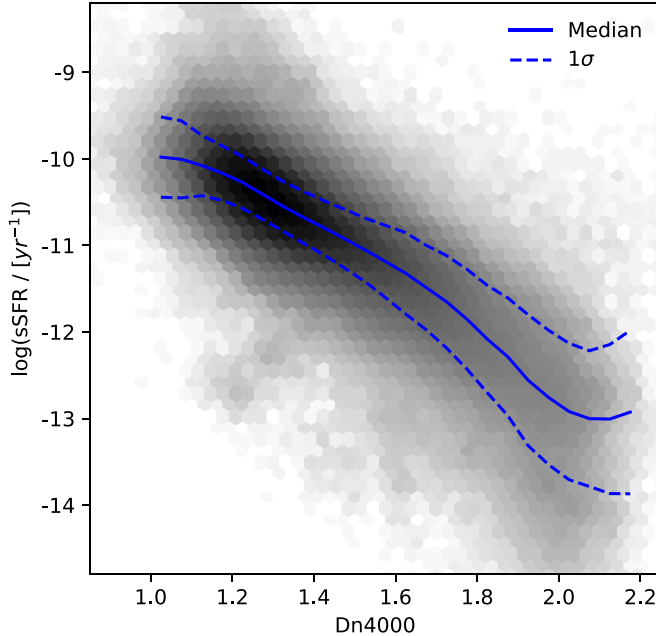


Figure A2. The two-dimensional histogram of resolved sSFR vs. Dn4000 for all MPL-6 spaxels with enough emission-line S/N. The sSFR is calculated from the AGN-removed H α luminosity, as described in Section 4.2.1. The gray colors represent the number density in a logarithm scale. The median relation is shown as the blue solid line. Blue dashed lines represent the 1σ dispersion. The average standard deviation of sSFR is about 0.6 dex. We note that the standard deviation is higher (about 0.8 dex) for high Dn4000 spaxels ($Dn4000 > 1.7$).

ORCID iDs

Gaoxiang Jin <https://orcid.org/0000-0003-3087-318X>
 Y. Sophia Dai <https://orcid.org/0000-0002-7928-416X>

Hsi-An Pan <https://orcid.org/0000-0002-1370-6964>
 Lihwai Lin <https://orcid.org/0000-0001-7218-7407>
 Cheng Li <https://orcid.org/0000-0002-8711-8970>
 Bau-Ching Hsieh <https://orcid.org/0000-0001-5615-4904>
 Shiyin Shen <https://orcid.org/0000-0002-3073-5871>
 Fang-Ting Yuan <https://orcid.org/0000-0001-6763-5869>
 Shuai Feng <https://orcid.org/0000-0002-9767-9237>
 Cheng Cheng <https://orcid.org/0000-0003-0202-0534>
 Hai Xu <https://orcid.org/0000-0003-1094-5190>
 Jia-Sheng Huang <https://orcid.org/0000-0001-6511-8745>
 Kai Zhang <https://orcid.org/0000-0002-9808-3646>

References

- Abazajian, K. N., Adelman-McCarthy, J. K., Agüeros, M. A., et al. 2009, *ApJS*, 182, 543
 Ackermann, S., Schawinski, K., Zhang, C., Weigel, A. K., & Turp, M. D. 2018, *MNRAS*, 479, 415
 Alonso, M. S., Lambas, D. G., Tissera, P., & Coldwell, G. 2007, *MNRAS*, 375, 1017
 Alonso, S., Coldwell, G., Duplancic, F., Mesa, V., & Lambas, D. G. 2018, *A&A*, 618, A149
 Alpaslan, M., Driver, S., Robotham, A. S. G., et al. 2015, *MNRAS*, 451, 3249
 Argudo-Fernández, M., Shen, S., Sabater, J., et al. 2016, *A&A*, 592, A30
 Astropy Collaboration, Robitaille, T. P., Tollerud, E. J., et al. 2013, *A&A*, 558, A33
 Baldwin, J. A., Phillips, M. M., & Terlevich, R. 1981, *PASP*, 93, 5
 Barnes, J. E. 1988, *ApJ*, 331, 699
 Barnes, J. E., & Hernquist, L. 1992, *ARA&A*, 30, 705
 Barnes, J. E., & Hernquist, L. E. 1991, *ApJL*, 370, L65
 Barrera-Ballesteros, J. K., García-Lorenzo, B., Falcón-Barroso, J., et al. 2015b, *A&A*, 582, A21
 Barrera-Ballesteros, J. K., Sánchez, S. F., García-Lorenzo, B., et al. 2015a, *A&A*, 579, A45
 Barton, E. J., Geller, M. J., & Kenyon, S. J. 2000, *ApJ*, 530, 660
 Belfiore, F., Maiolino, R., Bundy, K., et al. 2018, *MNRAS*, 477, 3014
 Belfiore, F., Westfall, K. B., Schaefer, A., et al. 2019, *AJ*, 158, 160

- Bennert, N., Canalizo, G., Jungwiert, B., et al. 2008, *ApJ*, **677**, 846
- Best, P. N., Kauffmann, G., Heckman, T. M., & Ivezic, Z. 2005, *MNRAS*, **362**, 9
- Binette, L., Magris, C. G., Stasińska, G., & Bruzual, A. G. 1994, *A&A*, **292**, 13
- Bing, L., Shi, Y., Chen, Y., et al. 2019, *MNRAS*, **482**, 194
- Blanton, M. R., Bershadsky, M. A., Abolfathi, B., et al. 2017, *AJ*, **154**, 28
- Bluck, A. F. L., Maiolino, R., Sánchez, S. F., et al. 2020, *MNRAS*, **492**, 96
- Blumenthal, K. A., & Barnes, J. E. 2018, *MNRAS*, **479**, 3952
- Bottrell, C., Hani, M. H., Teimoorinia, H., et al. 2019, *MNRAS*, **490**, 5390
- Brinchmann, J., Charlot, S., White, S. D. M., et al. 2004, *MNRAS*, **351**, 1151
- Bundy, K., Bershadsky, M. A., Law, D. R., et al. 2015, *ApJ*, **798**, 7
- Calzetti, D., Armus, L., Bohlin, R. C., et al. 2000, *ApJ*, **533**, 682
- Cano-Díaz, M., Ávila-Reese, V., Sánchez, S. F., et al. 2019, *MNRAS*, **488**, 3929
- Cao, C., Xu, C. K., Domingue, D., et al. 2016, *ApJS*, **222**, 16
- Capelo, P. R., Dotti, M., Volonteri, M., et al. 2017, *MNRAS*, **469**, 4437
- Cappellari, M. 2017, *MNRAS*, **466**, 798
- Cappellari, M., & Emsellem, E. 2004, *PASP*, **116**, 138
- Chang, Y.-Y., Le Floc'h, E., Juneau, S., et al. 2017, *ApJS*, **233**, 19
- Cherinka, B., Andrews, B. H., Sánchez-Gallego, J., et al. 2019, *AJ*, **158**, 74
- Cid Fernandes, R., Stasińska, G., Mateus, A., & Vale Asari, N. 2011, *MNRAS*, **413**, 1687
- Cid Fernandes, R., Stasińska, G., Schlickmann, M. S., et al. 2010, *MNRAS*, **403**, 1036
- Coil, A. L., Mendez, A. J., Eisenstein, D. J., & Moustakas, J. 2017, *ApJ*, **838**, 87
- Coldwell, G. V., & Lambas, D. G. 2006, *MNRAS*, **371**, 786
- Comerford, J. M., Negus, J., Müller-Sánchez, F., et al. 2020, *ApJ*, **901**, 159
- Cox, T. J., Jonsson, P., Somerville, R. S., Primack, J. R., & Dekel, A. 2008, *MNRAS*, **384**, 386
- Darg, D. W., Kaviraj, S., Lintott, C. J., et al. 2010, *MNRAS*, **401**, 1552
- de la Torre, S., Le Fèvre, O., Porciani, C., et al. 2011, *MNRAS*, **412**, 825
- Di Matteo, P., Combes, F., Melchior, A. L., & Semelin, B. 2007, *A&A*, **468**, 61
- Di Matteo, T., Springel, V., & Hernquist, L. 2005, *Natur*, **433**, 604
- Domínguez Sánchez, H., Huertas-Company, M., Bernardi, M., Tuccillo, D., & Fischer, J. L. 2018, *MNRAS*, **476**, 3661
- Donley, J. L., Kartaltepe, J., Kocevski, D., et al. 2018, *ApJ*, **853**, 63
- Dopita, M. A., Sutherland, R. S., Nicholls, D. C., Kewley, L. J., & Vogt, F. P. A. 2013, *ApJS*, **208**, 10
- Drory, N., MacDonald, N., Bershadsky, M. A., et al. 2015, *AJ*, **149**, 77
- Ellison, S. L., Mendel, J. T., Patton, D. R., & Scudder, J. M. 2013, *MNRAS*, **435**, 3627
- Ellison, S. L., Patton, D. R., Mendel, J. T., & Scudder, J. M. 2011, *MNRAS*, **418**, 2043
- Ellison, S. L., Patton, D. R., Simard, L., & McConnachie, A. W. 2008, *AJ*, **135**, 1877
- Ellison, S. L., Sánchez, S. F., Ibarra-Medel, H., et al. 2018, *MNRAS*, **474**, 2039
- Ellison, S. L., Viswanathan, A., Patton, D. R., et al. 2019, *MNRAS*, **487**, 2491
- Falcón-Barroso, J., Sánchez-Blázquez, P., Vazdekis, A., et al. 2011, *A&A*, **532**, A95
- Fan, L., Han, Y., Fang, G., et al. 2016, *ApJL*, **822**, L32
- Feng, S., Shen, S.-Y., Yuan, F.-T., et al. 2019, *ApJ*, **880**, 114
- Feng, S., Shen, S.-Y., Yuan, F.-T., Riffel, R. A., & Pan, K. 2020, *ApJL*, **892**, L20
- Fu, H., Steffen, J. L., Gross, A. C., et al. 2018, *ApJ*, **856**, 93
- Gabor, J. M., Capelo, P. R., Volonteri, M., et al. 2016, *A&A*, **592**, A62
- Gao, F., Wang, L., Pearson, W. J., et al. 2020, *A&A*, **637**, A94
- Geller, M. J., Kenyon, S. J., Barton, E. J., Jarrett, T. H., & Kewley, L. J. 2006, *AJ*, **132**, 2243
- Glikman, E., Simmons, B., Mailly, M., et al. 2015, *ApJ*, **806**, 218
- Goulding, A. D., Greene, J. E., Bezanson, R., et al. 2018, *PASJ*, **70**, S37
- Groves, B. A., Dopita, M. A., & Sutherland, R. S. 2004, *ApJS*, **153**, 9
- Guo, K., Peng, Y., Shao, L., et al. 2019, *ApJ*, **870**, 19
- Heckman, T. M., & Best, P. N. 2014, *ARA&A*, **52**, 589
- Hopkins, P. F., Hernquist, L., Cox, T. J., et al. 2006a, *ApJS*, **163**, 1
- Hopkins, P. F., Somerville, R. S., Hernquist, L., et al. 2006b, *ApJ*, **652**, 864
- Hou, M., Li, Z., & Liu, X. 2020, *ApJ*, **900**, 79
- Hwang, H. S., Elbaz, D., Dickinson, M., et al. 2011, *A&A*, **535**, A60
- Ji, X., & Yan, R. 2020, *MNRAS*, **499**, 5749
- Kartaltepe, J. S., Mozena, M., Kocevski, D., et al. 2015, *ApJS*, **221**, 11
- Kauffmann, G., & Haehnelt, M. 2000, *MNRAS*, **311**, 576
- Kauffmann, G., & Heckman, T. M. 2009, *MNRAS*, **397**, 135
- Kauffmann, G., Heckman, T. M., Tremonti, C., et al. 2003, *MNRAS*, **346**, 1055
- Kauffmann, G., White, S. D. M., Heckman, T. M., et al. 2004, *MNRAS*, **353**, 713
- Keel, W. C., Kennicutt, R. C., J., Hummel, E., & van der Hulst, J. M. 1985, *AJ*, **90**, 708
- Kennicutt, R. C., & Evans, N. J. 2012, *ARA&A*, **50**, 531
- Kennicutt, Robert C., J., Keel, W. C., van der Hulst, J. M., Hummel, E., & Roettiger, K. A. 1987, *AJ*, **93**, 1011
- Kewley, L. J., & Dopita, M. A. 2002, *ApJS*, **142**, 35
- Kewley, L. J., Dopita, M. A., Sutherland, R. S., Heisler, C. A., & Trevena, J. 2001, *ApJ*, **556**, 121
- Knapen, J. H., & James, P. A. 2009, *ApJ*, **698**, 1437
- Lackner, C. N., Silverman, J. D., Salvato, M., et al. 2014, *AJ*, **148**, 137
- Lambas, D. G., Tissera, P. B., Alonso, M. S., & Coldwell, G. 2003, *MNRAS*, **346**, 1189
- Larson, R. B., & Tinsley, B. M. 1978, *ApJ*, **219**, 46
- Law, D. R., Yan, R., Bershadsky, M. A., et al. 2015, *AJ*, **150**, 19
- Li, C., Kauffmann, G., Heckman, T. M., Jing, Y. P., & White, S. D. M. 2008a, *MNRAS*, **385**, 1903
- Li, C., Kauffmann, G., Heckman, T. M., White, S. D. M., & Jing, Y. P. 2008b, *MNRAS*, **385**, 1915
- Li, C., Kauffmann, G., Jing, Y. P., et al. 2006, *MNRAS*, **368**, 21
- Li, S.-I., Shi, Y., Bizyaev, D., et al. 2021, *MNRAS*, **501**, 14
- Lin, L., Belfiore, F., Pan, H.-A., et al. 2017, *ApJ*, **851**, 18
- Lin, L., Koo, D. C., Weiner, B. J., et al. 2007, *ApJL*, **660**, L51
- Lin, L., Koo, D. C., Willmer, C. N. A., et al. 2004, *ApJL*, **617**, L9
- Liu, X., Shen, Y., & Strauss, M. A. 2012, *ApJ*, **745**, 94
- Moreno, J., Torrey, P., Ellison, S. L., et al. 2015, *MNRAS*, **448**, 1107
- Muldrew, S. I., Croton, D. J., Skibba, R. A., et al. 2012, *MNRAS*, **419**, 2670
- Noeske, K. G., Weiner, B. J., Faber, S. M., et al. 2007, *ApJL*, **660**, L43
- Norberg, P., Baugh, C. M., Hawkins, E., et al. 2002, *MNRAS*, **332**, 827
- Oke, J. B., & Gunn, J. E. 1983, *ApJ*, **266**, 713
- Osterbrock, D. E., & Ferland, G. J. 2006, *Astrophysics of Gaseous Nebulae and Active Galactic Nuclei* (Sausalito, CA: Univ. Science Books)
- Padovani, P., Alexander, D. M., Assef, R. J., et al. 2017, *A&ARv*, **25**, 2
- Pan, H.-A., Lin, L., Hsieh, B.-C., et al. 2018, *ApJ*, **854**, 159
- Pan, H.-A., Lin, L., Hsieh, B.-C., et al. 2019, *ApJ*, **881**, 119
- Patton, D. R., & Atfield, J. E. 2008, *ApJ*, **685**, 235
- Patton, D. R., Ellison, S. L., Simard, L., McConnachie, A. W., & Mendel, J. T. 2011, *MNRAS*, **412**, 591
- Patton, D. R., Grant, J. K., Simard, L., et al. 2005, *AJ*, **130**, 2043
- Patton, D. R., Pritchett, C. J., Carlberg, R. G., et al. 2002, *ApJ*, **565**, 208
- Pearson, W. J., Wang, L., Trayford, J. W., Petrucci, C. E., & van der Tak, F. F. S. 2019, *A&A*, **626**, A49
- Rembold, S. B., Shimoia, J. S., Storchi-Bergmann, T., et al. 2017, *MNRAS*, **472**, 4382
- Rosario, D. J., Mendel, J. T., Ellison, S. L., Lutz, D., & Trump, J. R. 2016, *MNRAS*, **457**, 2703
- Saintonge, A., Catinella, B., Tacconi, L. J., et al. 2017, *ApJS*, **233**, 22
- Salim, S., Rich, R. M., Charlot, S., et al. 2007, *ApJS*, **173**, 267
- Salpeter, E. E. 1955, *ApJ*, **121**, 161
- Sánchez, S. F. 2020, *ARA&A*, **58**, 99
- Sánchez, S. F., Avila-Reese, V., Hernandez-Toledo, H., et al. 2018, *RMxAA*, **54**, 217
- Sánchez, S. F., Pérez, E., Sánchez-Blázquez, P., et al. 2016a, *RMxAA*, **52**, 21
- Sánchez, S. F., Pérez, E., Sánchez-Blázquez, P., et al. 2016b, *RMxAA*, **52**, 171
- Sánchez-Blázquez, P., Peletier, R. F., Jiménez-Vicente, J., et al. 2006, *MNRAS*, **371**, 703
- Sanders, D. B., & Mirabel, I. F. 1996, *ARA&A*, **34**, 749
- Satyapal, S., Ellison, S. L., McAlpine, W., et al. 2014, *MNRAS*, **441**, 1297
- Schmidt, K. B., Rix, H.-W., da Cunha, E., et al. 2013, *MNRAS*, **432**, 285
- Schmitt, H. R. 2001, *AJ*, **122**, 2243
- Scudder, J. M., Ellison, S. L., Momjian, E., et al. 2015, *MNRAS*, **449**, 3719
- Secrest, N. J., Ellison, S. L., Satyapal, S., & Blecha, L. 2020, *MNRAS*, **499**, 2380
- Shah, E. A., Kartaltepe, J. S., Magagnoli, C. T., et al. 2020, *ApJ*, **904**, 107
- Shao, L., Li, C., Kauffmann, G., & Wang, J. 2015, *MNRAS*, **448**, L72
- Shen, S.-Y., Argudo-Fernández, M., Chen, L., et al. 2016, *RAA*, **16**, 43
- Silva, A., Marchesini, D., Silverman, J. D., et al. 2021, *ApJ*, **909**, 124
- Silverman, J. D., Kampezyk, P., Jahnke, K., et al. 2011, *ApJ*, **743**, 2
- Sinha, M., & Holley-Bockelmann, K. 2012, *ApJ*, **751**, 17
- Skibba, R. A., Bamford, S. P., Nichol, R. C., et al. 2009, *MNRAS*, **399**, 966
- Smith, B. J., & Struck, C. 2010, *AJ*, **140**, 1975
- Spindler, A., Wake, D., Belfiore, F., et al. 2018, *MNRAS*, **476**, 580
- Steffen, J. L., Fu, H., Comerford, J. M., et al. 2021, *ApJ*, **909**, 120
- Thorp, M. D., Ellison, S. L., Simard, L., Sánchez, S. F., & Antonio, B. 2019, *MNRAS*, **482**, L55

- Toomre, A. 1977, in Evolution of Galaxies and Stellar Populations, ed. B. M. Tinsley, D. C. Larson, & Richard B. Gehret (New Haven, CT: Yale Univ. Press), 401
- Toomre, A., & Toomre, J. 1972, *ApJ*, 178, 623
- Torrey, P., Cox, T. J., Kewley, L., & Hernquist, L. 2012, *ApJ*, 746, 108
- Trump, J. R., Sun, M., Zeimann, G. R., et al. 2015, *ApJ*, 811, 26
- Urrutia, T., Lacy, M., & Becker, R. H. 2008, *ApJ*, 674, 80
- Veilleux, S., Kim, D. C., Rupke, D. S. N., et al. 2009, *ApJ*, 701, 587
- Veilleux, S., Kim, D. C., & Sanders, D. B. 2002, *ApJS*, 143, 315
- Veilleux, S., & Osterbrock, D. E. 1987, *ApJS*, 63, 295
- Violino, G., Ellison, S. L., Sargent, M., et al. 2018, *MNRAS*, 476, 2591
- Wake, D. A., Bundy, K., Diamond-Stanic, A. M., et al. 2017, *AJ*, 154, 86
- Walmsley, M., Ferguson, A. M. N., Mann, R. G., & Lintott, C. J. 2019, *MNRAS*, 483, 2968
- Wang, E., Li, C., Xiao, T., et al. 2018, *ApJ*, 856, 137
- Wang, E., Lilly, S. J., Pezzulli, G., & Matthee, J. 2019, *ApJ*, 877, 132
- Wang, H., Mo, H. J., Jing, Y. P., et al. 2009, *MNRAS*, 394, 398
- Westfall, K. B., Cappellari, M., Bershady, M. A., et al. 2019, *AJ*, 158, 231
- Weston, M. E., McIntosh, D. H., Brodwin, M., et al. 2017, *MNRAS*, 464, 3882
- Wild, V., Rosales-Ortega, F., Falcón-Barroso, J., et al. 2014, *A&A*, 567, A132
- Willett, K. W., Lintott, C. J., Bamford, S. P., et al. 2013, *MNRAS*, 435, 2835
- Woods, D. F., & Geller, M. J. 2007, *AJ*, 134, 527
- Woods, D. F., Geller, M. J., & Barton, E. J. 2006, *AJ*, 132, 197
- Woods, D. F., Geller, M. J., Kurtz, M. J., et al. 2010, *AJ*, 139, 1857
- Wyder, T. K., Martin, D. C., Schiminovich, D., et al. 2007, *ApJS*, 173, 293
- Wylezalek, D., Zakamska, N. L., Greene, J. E., et al. 2018, *MNRAS*, 474, 1499
- Xu, C., & Sulentic, J. W. 1991, *ApJ*, 374, 407
- Xu, C. K., Domingue, D., Cheng, Y.-W., et al. 2010, *ApJ*, 713, 330
- Yan, R., & Blanton, M. R. 2012, *ApJ*, 747, 61
- Yan, R., Bundy, K., Law, D. R., et al. 2016b, *AJ*, 152, 197
- Yan, R., Tremonti, C., Bershady, M. A., et al. 2016a, *AJ*, 151, 8
- Yang, X., Mo, H. J., van den Bosch, F. C., et al. 2007, *ApJ*, 671, 153
- Yuan, F.-T., Argudo-Fernández, M., Shen, S., et al. 2018, *A&A*, 613, A13
- Yuan, F. T., Takeuchi, T. T., Matsuoka, Y., et al. 2012, *A&A*, 548, A117
- Zehavi, I., Zheng, Z., Weinberg, D. H., et al. 2005, *ApJ*, 630, 1